**Title:** miR-1 coordinately regulates lysosomal v-ATPase and biogenesis to affect muscle contractility upon proteotoxic challenge during ageing

[1, 8]Isabelle Schiffer, [1, 8]Birgit Gerisch, [1, 8]Kazuto Kawamura, [1]Raymond Laboy, [1, 3]Jennifer Hewitt, [1, 2]Martin S. Denzel, [4, 5, 6]Marcelo A. Mori, [3]Siva Vanapalli, [7]Yidong Shen, [1]Orsolya Symmons, [1, 2, 9]Adam Antebi

[1]Max Planck Institute for Biology of Ageing, Joseph Stelzmann Str. 9b, 50931, Cologne, Germany
[2]Cologne Excellence Cluster on Cellular Stress Responses in Aging-Associated Diseases (CECAD), University of Cologne, 50931, Cologne, Germany
[3]Department of Chemical Engineering, Texas Tech University, Lubbock, TX 79409, USA
[4]Laboratory of Aging Biology, Department of Biochemistry and Tissue Biology, University of Campinas (UNICAMP), Campinas, Brazil
[5]Experimental Medicine Research Cluster (EMRC), University of Campinas (UNICAMP), Campinas, Brazil
[6]Obesity and Comorbidities Research Center (OCRC), University of Campinas (UNICAMP), Campinas, Brazil
[7]State Key Laboratory of Cell Biology, Innovation Center for Cell Signaling Network, CAS Center for Excellence in Molecular Cell Science, Shanghai Institute of Biochemistry and Cell Biology, Chinese Academy of Sciences, University of Chinese Academy of Sciences
[8]co-first author
[9]corresponding author

Correspondence: aantebi@age.mpg.de

**Abstract**

Muscle function relies on the precise architecture of dynamic contractile elements, which must be fine-tuned to maintain motility throughout life. Muscle is also highly plastic, and remodelled in response to stress, growth, neural and metabolic inputs. The evolutionarily conserved muscle-enriched microRNA, miR-1, regulates distinct aspects of muscle biology during development, but whether it plays a role during ageing is unknown. Here we investigated the role of *C. elegans* miR-1 in muscle function in response to proteostatic stress during adulthood. *mir-1* deletion results in improved mid-life muscle motility, pharyngeal pumping, and organismal longevity under conditions of polyglutamine repeat proteotoxic challenge. We identified multiple vacuolar ATPase subunits as subject to miR-1 control, and the regulatory subunit *vha-13*/ATP6VIA as a direct target downregulated via its 3'UTR to mediate miR-1 physiology. miR-1 further regulates nuclear localization of lysosomal biogenesis factor HLH-30/TFEB and lysosomal acidification. In summary, our studies reveal that miR-1 coordinately regulates lysosomal v-ATPase and biogenesis to impact muscle function and health during ageing.

## Introduction

Ageing is the major cause of progressive decline in all organ systems throughout the body. This is particularly evident in the musculature and often manifests as sarcopenia, the loss of muscle mass and strength. In fact, muscle frailty is a hallmark of tissue ageing seen in species as diverse as worms, flies, mice and humans (Herndon et al., 2002; Miller et al., 2008) (V. G. Martinez et al., 2007) (Demontis, Piccirillo, Goldberg, & Perrimon, 2013) (Cruz-Jentoft et al., 2010) (Nair, 2005). At the molecular level, frailty is often accompanied by a decline in muscle structure and function, as well as alterations in muscle proteostasis and metabolism. Nevertheless, muscle can respond positively to exercise and stress and rejuvenate even into older age, showing remarkable plasticity (Pollock et al., 2018) (Cartee, Hepple, Bamman, & Zierath, 2016) (Distefano & Goodpaster, 2018). A molecular study of muscle ageing and plasticity in a genetically tractable model could shed light on fundamental aspects of these processes.

microRNAs are small 22-26 nucleotide RNAs that bind with complementarity through their seed sequence to target mRNAs to downregulate gene expression (Gu & Kay, 2010). They can work as molecular switches or fine tune gene regulation, and typically have multiple targets, thereby coordinating cellular programs. Many microRNAs are expressed in a tissue-specific manner and regulate programs cell autonomously, and could therefore potentially serve as tissue-specific therapeutic targets (Guo et al., 2014) (Panwar, Omenn, & Guan, 2017). In addition, some microRNAs are found circulating in serum (Weber et al., 2010) (Chen et al., 2008), raising the possibility that they can act cell non-autonomously as well.

miR-1 homologs are muscle-enriched microRNAs that are highly conserved in evolution, and important for mammalian heart and muscle development (Zhao et al., 2007). Like in other animals, *Caenorhabditis elegans mir-1* is expressed in body wall ("skeletal") and pharyngeal ("cardiac") muscle (Simon et al., 2008). Deletion mutants are viable and exhibit modest changes in the behavior of the neuromuscular junction (Simon et al., 2008) and autophagy (Nehammer et al., 2019), but little else is known of its normative function. In this work, we examined the potential role of miR-1 in regulating muscle function and proteostasis. Surprisingly, we found that under polyQ35 proteotoxic challenge, *mir-1* mutation prevents aggregate formation, and increases organismal motility and pharyngeal contractility during ageing. Mechanistically, miR-1

regulates expression of several lysosomal v-ATPase subunits, and targets a crucial regulatory component, *vha-13*/ATP6VIA, via its 3' UTR to impact proteotoxicity and longevity. Further, miR-1 regulates lysosomal acidification and nuclear localization of HLH-30/TFEB, a key regulator of lysosome biogenesis. These studies reveal an unexpected role of miR-1 in coordinating lysosomal function and health during ageing.

## Results

### *mir-1* mutation improves muscle motility upon polyQ challenge

*mir-1* is a highly conserved microRNA expressed predominantly in muscle tissues including pharyngeal muscle, body wall muscle, and sex muscles (Andachi & Kohara, 2016; N. J. Martinez et al., 2008). To unravel molecular miR-1 function, we first characterized the nature of several *mir-1* mutations. The reference alleles (*n4101, n4102*) consist of large deletions of the region that could have confounding effects on nearby loci. We therefore focused on *gk276*, a smaller 192 base pair deletion that removes the *mir-1* coding region as well as the downstream non-coding region. We also generated an independent *mir-1* allele, *dh1111,* by CRISPR genome engineering (Figure 1A), which deletes a 52 base pair region within the *mir-1* locus. Both alleles failed to express the mature miRNA as measured by Taqman qPCR (Supplemental Figure 1A), and thus are *mir-1* null mutants.

To investigate *mir-1* function, we measured several physiological parameters. We found that *mir-1* mutants *gk276* and *dh1111* developed normally, had normal brood size, and near normal life span (Supplemental Figure 1B-D, Supplemental Table 1). Additionally, motility on solid media, thrashing in liquid culture, and pharyngeal pumping ability determined at day 8 and 14 of adulthood were similar to wild-type N2 controls (Supplemental Figure 1E-G, Supplemental Table 2). Since *mir-1* deletion showed little obvious phenotype on its own, we reasoned that some physiological differences might emerge under stress. However, we saw little distinction from wild-type (WT) with moderate heat stress by growth at 25°C nor heat shock resistance at 35°C (Supplemental Figure 1D and H, Supplemental Table 1).

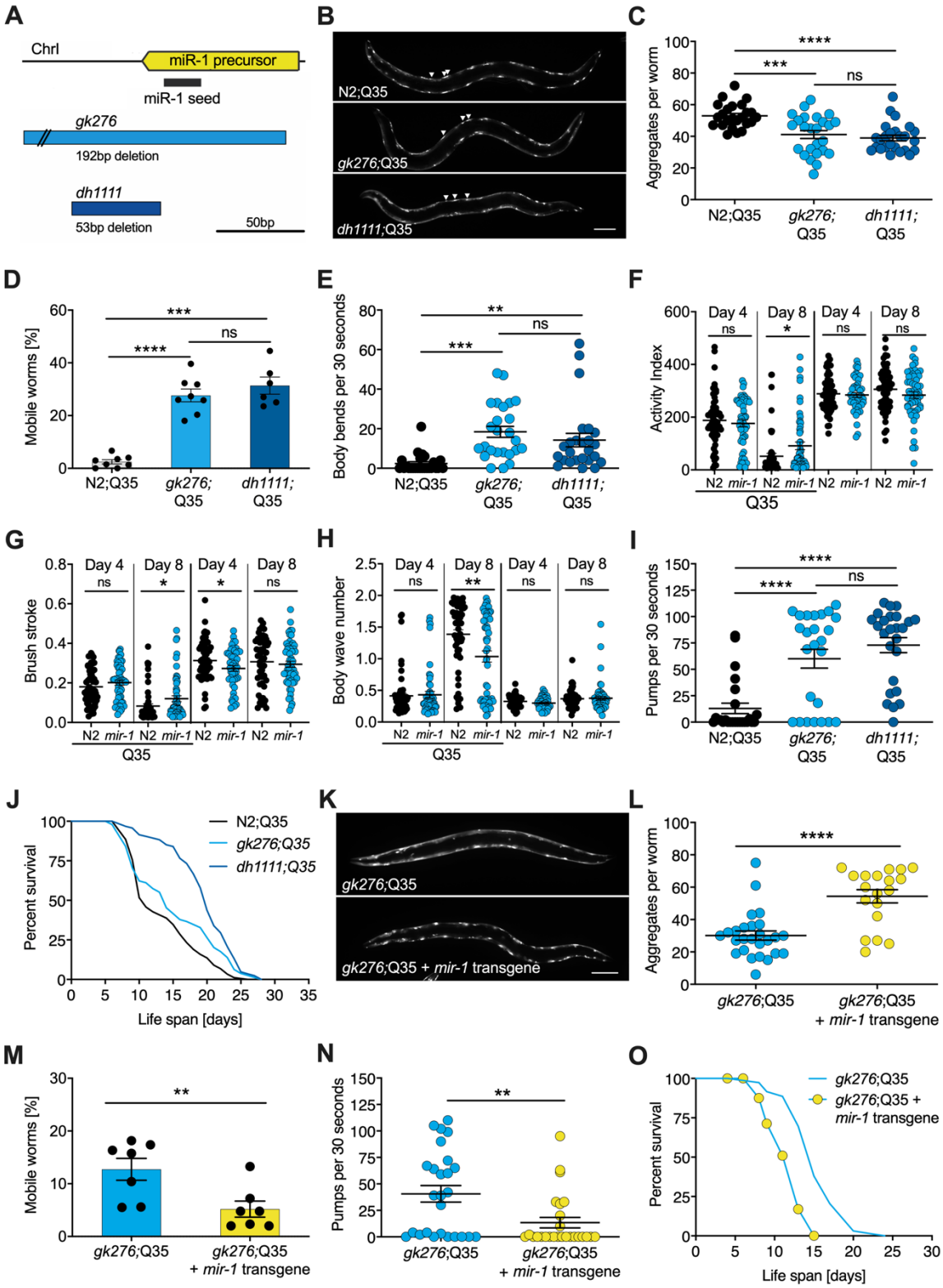


**Figure 1. *mir-1* mutants exhibit improved motility upon polyQ challenge.**

**(A)** Schematic showing the *mir-1* locus, deletion alleles *mir-1(gk276)* and *mir-1(dh1111)* (see Material and Methods).

**(B)** Representative images of wild-type N2 and *mir-1* mutant animals expressing *unc-54p::Q35::YFP* (Q35) showing loss of aggregates in the *mir-1* background on day 4 of adulthood. Arrowheads point to aggregates. Scale bar 100 µm. **(C)** Quantification of *Q35::YFP* aggregates in B using Zen software,

each dot represents one animal, mean ± SEM from one representative experiment, N=3, one way ANOVA, Tukey´s multiple comparisons test, ***, p<0.001, ****, p<0.000, ns, not significant.
**(D)** Motility of indicated *mir-1* alleles and wild-type animals expressing *unc-54p::Q35::YFP*, measured by the circle test, day 8 of adulthood. Percent worms that left the circle after 30 minutes was determined. Each dot represents one experiment. Mean ± SEM of N=6 to 8. One way ANOVA, ***, p<0.001, ****, p<0.0001, ns, not significant.
**(E)** Motility of *mir-1* alleles and wild-type animals expressing *unc-54p::Q35::YFP*, measured by the thrashing assay. 25 worms per condition, each dot represents one animal, mean ± SEM from one representative experiment, N=4, one way ANOVA, **, p<0.01 ***, p<0.001, ns, not significant.
CeleST analysis of activity index **(F)**, brush stroke **(G)** and body wave **(H)** comparing N2 and *mir-1(gk276)* mutant animals with or without *unc-54p::Q35::YFP* at day 4 and day 8 of adulthood. Each dot represents one animal. t-test, *, p<0.05 **, p<0.01, ns, not significant.
**(I)** Pharyngeal pumping rate measured on day 8 of adulthood in *mir-1* alleles and wild-type animals expressing *unc-54p::Q35::YFP.* Each dot represents one animal, mean ± SEM from one representative experiment, N=3, one way ANOVA, ****, p<0.0001, ns, not significant.
**(J)** Life span experiments of *mir-1* mutants and wild-type animals expressing *unc-54P::Q35::YFP.* One experiment of N=3. t-test: N2;Q35 *vs. gk276*;Q35: p=0.03. N2;Q35 *vs. dh1111*;Q35: p<0.0001.
**(K)** Presence of an extrachromosomal *mir-1* transgene brings back aggregates in *mir-1(gk276)* mutants at day 4 of adulthood, showing rescue by the transgene. Transgenic worms were compared to non-transgenic segregants of the same strain. Scale bar 100 µm. **(L)** Quantification of *Q35::YFP* aggregates (from **K**), each dot represents total aggregate number of one animal, mean ± SEM from one representative experiment, N=3, t-test, ****, p<0.0001.
**(M)** Motility of *mir-1(gk276) unc-54p::Q35::YFP* animals in the presence or absence of the *mir-1* transgene at day 8 of adulthood, measured by circle test. Each dot represents one experiment, mean ± SEM of N=7. Total number of worms tested 646 (transgenic worms) and 469 (non-transgenic segregants of the same strain), t-test, **, p<0.01.
**(N)** Pharyngeal pumping rate of *mir-1(gk276) unc-54p::Q35::YFP* animals in the presence or absence of the *mir-1* transgene. Transgenic worms were compared to non-transgenic segregants of the same strain. Each dot represents one animal, mean ± SEM from one representative experiment, N=7, t-test, **, p<0.01.
(**O**) Life span experiments of *mir-1(gk276) unc-54p::Q35::YFP* animals in the presence or absence of the *mir-1* transgene. Transgenic worms were compared to non-transgenic segregants of the same strain. One representative experiment of N=5, t-test, p<0.0001.

We next tested the idea that *mir-1* mutants might differ in their response to proteotoxic stress. To do so, we used a strain expressing polyglutamine-35 tracts fused to yellow fluorescent protein (YFP) under the control of the muscle myosin specific *unc-54* promoter (*unc-54p::Q35::YFP*), which has been used previously in models of proteotoxicity and Huntington's disease (Morley, Brignull, Weyers, & Morimoto, 2002)

(Brignull, Morley, Garcia, & Morimoto, 2006). In these strains, initially soluble proteins become sequestered into insoluble aggregates, visible as foci in the muscle of the worm. Worms expressing the polyQ35 stretches showed progressive age-dependent protein aggregation, which became clearly visible by day 4 of adulthood. Interestingly, we observed that *mir-1* mutants displayed significantly less aggregates (avg. 38 and 36) compared to age-matched wild-type controls (avg. 53) at this time (Figure 1B and C, Supplemental Table 2).

We further investigated the possible effect of proteotoxicity by measuring organismal motility of Q35 strains using the circle test. This test measures how many worms crawl out of a 1 cm circle within 30 minutes on day 8 of adulthood on agar plates. Day 8 was chosen as a timepoint where paralysis becomes visible but animals are still viable. We observed that about 30% of the *mir-1;*Q35 mutants left the circle while only 2.5% of the control Q35 worms did so (Figure 1D, Supplemental Table 2). We also measured motility by counting the thrashing rate in liquid culture on day 8 of adulthood. Though the degree of paralysis was more variable, both *mir-1* mutants *gk276* and *dh1111* were significantly more mobile (average 16, 15 body bends) compared to age-matched wild-type controls (average 2 body bends, Figure 1E, Supplemental Table 2).

To further characterize miR-1's impact on muscle function, we performed CeleST analysis (Restif et al., 2014), a MATLAB based algorithm that extracts various parameters of movement (wave initiation, travel speed, brush stroke, activity index) and gait (wave number, asymmetry, curl, stretch) from video footage. Typically activity measures decline with age, whereas gait abnormalities increase with age (Restif et al., 2014). We scored animals focusing on day 4 and 8 of adulthood comparing *mir-1* and WT, in the presence and absence of the Q35 array. In the absence of Q35, *mir-1* mutants performed similar to WT (*e.g.*, body wave) or were slightly different (wave initiation, travel speed, stretch) for some parameters (Supplemental Table 3). In the presence of Q35, however, *mir-1* mutants did significantly better than WT for several measures of activity (activity index, brush stroke, travel speed, wave initiation) and gait (body wave) on day 8 (Figure 1F-H, Supplemental Figure 1I-M, Supplemental Table 3), consistent with the idea that *mir-1* mutation protects against proteotoxic stress during mid-life.

*mir-1* is also highly expressed in the pharynx, a contractile tissue similar to cardiac muscle. We observed that in the *mir-1*;Q35 background, pumping rate was significantly increased (*gk276*, avg. 60; *dh1111*, avg. 78) compared to Q35 controls (avg. 16) on day 8 of adulthood (Figure 1I, Supplemental Table 2). Furthermore, we found that the life span of *mir-1(dh1111)*;Q35 strains was significantly extended (n=3, mean 13 (WT) vs.19 (*dh1111*) days) compared to Q35 alone (Figure 1J, Supplemental Table 1). A similar trend was seen with *gk276* in 2 of 3 experiments (Figure 1J, Supplemental Table 1). These findings suggest that *mir-1* reduction can counter the intrinsic and systemic detrimental effects of Q35 proteotoxic challenge.

Introducing a wild-type *mir-1* transgene into the *mir-1(gk276)* background restored normal levels of *mir-1* expression (Supplemental Figure 1N) and largely reversed *mir-1* phenotypes, showing increased Q35 aggregates, decreased motility, pumping rate, and life span compared to non-transgenic controls (Figure 1K-O, Supplemental Table 1 and 2). The similarity of behaviour among the different *mir-1* alleles and the rescue of these phenotypes by the wild-type transgene demonstrate that the *mir-1* mutation is causal for removing muscle aggregates and improving mid-life motility.

**v-ATPase subunits are downstream mediators of miR-1 induced motility improvement**

To identify downstream mediators of protein quality control improvement in *mir-1* mutants, we used computational and proteomic approaches to find potential miR-1 targets. For the computational approach, we used publicly available prediction tools to identify genes harbouring miR-1 seed binding sites in their 3'UTR, namely microRNA.org, TargetScanWorm, and PicTar (Betel, Wilson, Gabow, Marks, & Sander, 2008) (Jan, Friedman, Ruby, & Bartel, 2011) (Lall et al., 2006). These prediction tools use distinct algorithms that often yield different and extensive sets of candidates (Figure 2A). Therefore, we limited ourselves mostly to candidates that were predicted as targets by all three algorithms. This yielded 68 overlapping candidates (Figure 2A), 50 of which had available RNAi clones (Supplementary Table 4). Interestingly, network analysis of these 68 genes using STRING (string-db.org) (Snel, Lehmann, Bork, & Huynen, 2000) revealed a tight cluster of predicted targets encoding 11/21 subunits of the vacuolar ATPase (Figure 2B, Supplemental Figure S2A). 5

additional vacuolar ATPase genes were identified by 2 of the 3 prediction algorithms (Supplemental Figure 2A). In addition, two genes that code transcription factors implicated in lysosome biogenesis, *daf-16*/FOXO and *hlh-30*/TFEB (Sardiello et al., 2009; Settembre et al., 2011), also contained predicted miR-1 binding sites in their 3'UTRs.

Next, we carried out a functional screen of the selected candidates. We reasoned that *mir-1* deletion likely results in an upregulation of these proteins, and that RNAi knockdown of the relevant genes should therefore abrogate the improved motility of *mir-1*;Q35 worms. Specifically, we scored motility using a rapid version of the circle test, measuring the ability of *mir-1*;Q35 worms grown on candidate RNAis to migrate out of a 1 cm diameter circle within 1 minute (Figure 2C). 12/20 *mir-1*;Q35 worms left the circle when grown on luciferase control RNAi (*luci)*. We considered genes as potential *mir-1*;Q35 suppressors if less then 4 worms left the circle upon RNAi knock down of the genes, and prioritized candidates when only 0 or 1 worms left. Among the selected candidates vacuolar ATPase subunits *vha-1, vha-8, vha-9, vha-13,* and *vha-14*, as well as muscle gene *zyx-1*, stood out as molecules suppressing *mir-1* motility (Figure 2C and Supplemental Figure 2D).

As a second parallel approach to identify miR-1 regulatory targets in an unbiased manner, we performed TMT shotgun proteomic analysis, comparing *mir-1* mutants to WT worms on day 1 of adulthood. We identified approximately 1,500-2,000 proteins in the replicates (Figure 2D). Samples showed a high degree of correlation (Supplemental Figure 2B) with minimal separation of WT and *mir-1* genotypes, reflecting the subtle changes induced by *mir-1* mutation at the organismal level. For further analysis we therefore selected the 50 top upregulated proteins with available RNAi clones and tested them for their ability to suppress the motility phenotype using the circle test (Supplemental Figure 2C and 2E, Supplemental Table 5), among them *vha-10*, *vha-19* and *zyx-1*, which had previously been predicted to harbour *mir-1* binding sites.

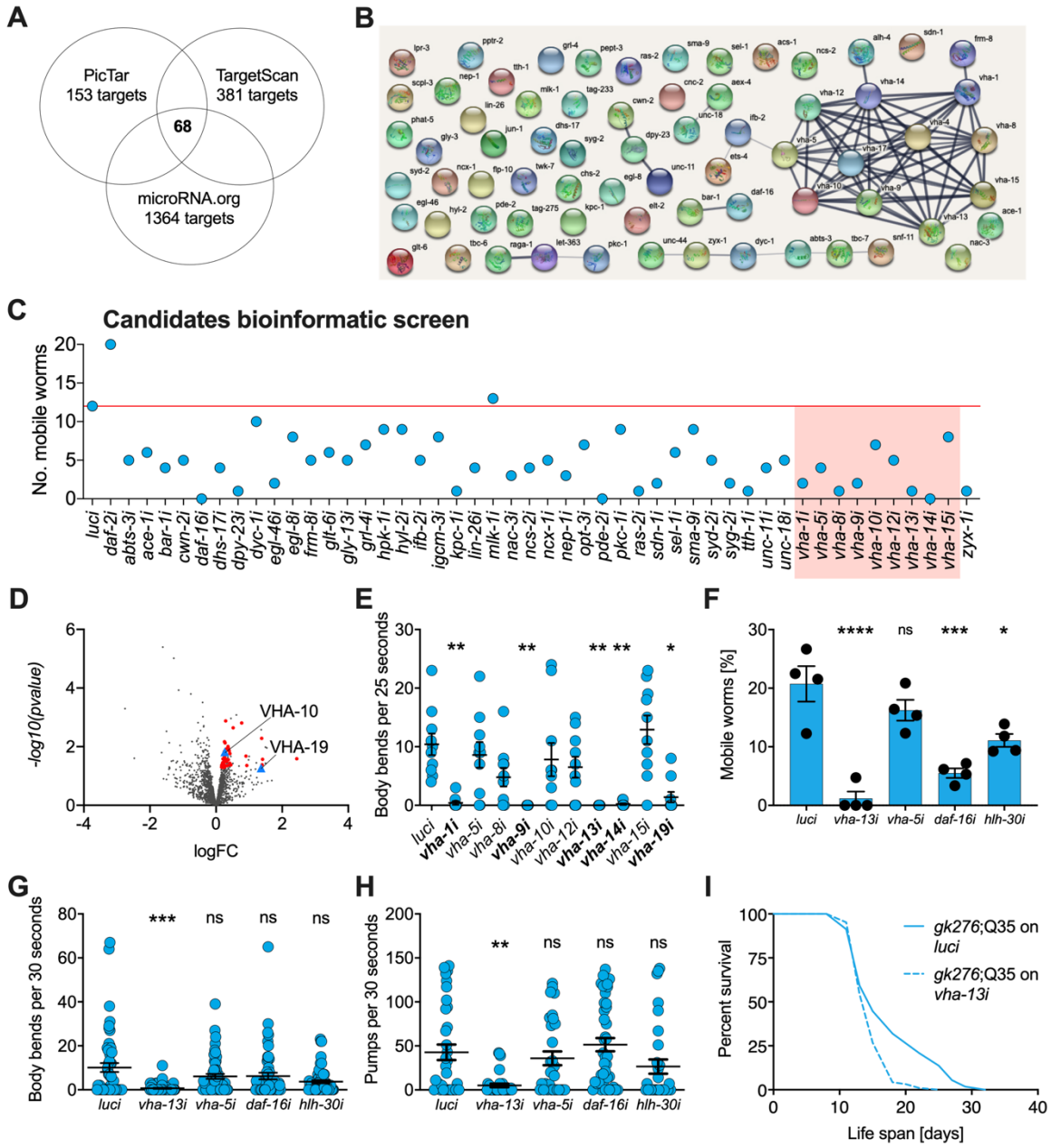


**Figure 2. v-ATPase subunits are downstream mediators of *mir-1* induced motility improvement.**

**(A)** Computational screen using *in silico* prediction of miR-1 binding sites in target mRNAs using microRNA.org, TargetScan and PicTar identifies 68 shared candidates.

**(B)** STRING network analysis of predicted miR-1 targets reveals a cluster of vATPase subunits.

**(C)** Initial RNAi screen of computationally predicted candidates using the circle test on day 8 of adulthood reveals a number of candidates that reduced motility of *mir-1(gk276)*;Q35, 20 worms per RNAi (N=1). Red line, number of luciferase controls that left the circle. v-ATPases are highlighted in red.

**(D)** Volcano plot of proteomic analysis showing differentially regulated proteins in *mir-1* vs. N2 animals. Red dots show upregulated proteins tested in circle assay, VHA-10 and VHA-19 indicated by blue triangles. N=6 (*mir-1*) and 4 (N2) biological replicates.

**(E)** Effect of v-ATPase subunit RNAi knockdown on *mir-1(gk276)*;Q35 motility as measured in the thrashing assay. Animals are grown on the corresponding RNAi from L4 onwards. N=1. Mean ± SEM, one way ANOVA, only significant values are labelled: *, p<0.05, **, p<0.01.
**(F)** and **(G)** Motility assay (circle test) and trashing assay on day 8 of *mir-1(gk276)*;Q35 worms upon *vha-13, vha-5, daf-16 and hlh-30* RNAi knockdown. Control, luciferase RNAi (*luci*). Mean ± SEM of N=4, one way ANOVA, *, p<0.05, ***, p<0.001, ****, p<0.0001, ns, not significant.
**(H)** Pumping assay of *mir-1(gk276)*;Q35 worms upon *vha-13, vha-5, daf-16 and hlh-30* RNAi knockdown on day 8 of adulthood. Control, luciferase RNAi (*luci*). N=3, mean ± SEM, one way ANOVA, **, p<0.01, ns, not significant.
**(I)** Life span of *mir-1*;Q35 and Q35 worms upon *vha-13* RNAi knockdown. One experiment of N=3, t-test: p<0.01.

Based on the prominent presence of vATPase genes among both the informatic and the proteomic candidates, we systematically tested 10 of them in the thrashing assay, confirming v-ATPase subunits *vha-1, vha-9, vha-13, vha-14* and *vha-19* as likely mediators of *mir-1*;Q35 motility (Figure 2E). We further tested the impact of *vha-5, vha-13* and transcription factors *daf-16/FOXO* and *hlh-30/TFEB* RNAi *on mir-1*;Q35 phenotypes in more detail, using the circle test, thrashing assay and pharyngeal pumping as readout (Figure 2F-H), which again confirmed in particular the role of *vha-13* in reducing *mir-1* motility. We also confirmed that the effect on motility was specific to the *mir-1* background for *vha-5*, *vha-10*, *vha-13* and *hlh-30*, since RNAi of these genes had no significant effect on motility in N2;Q35 worms (Supplemental Figure 2F).

In summary, knockdown of 5 of 10 tested v-ATPase subunits from both the computational and proteomics screen, as well as 2 transcriptional mediators of lysosome biogenesis, reduced or abolished *mir-1* motility improvement either by circle test or thrashing, revealing these molecules to have congruent physiological effects. Therefore, we focused most of our further efforts on examining v-ATPase regulation by miR-1.

## miR-1 directly regulates VHA-13 protein levels in muscle tissue

MicroRNAs regulate their targets by binding to the 3' UTR of client mRNAs, thereby decreasing RNA stability and translation. If miR-1 regulates v-ATPase subunits, then miR-1 loss would be predicted to de-repress v-ATPase mRNA and

protein levels. Because the onset of Q35 aggregation becomes visible by day 4 of adulthood, we examined the mRNA expression of representative v-ATPase subunits at this time. We found that the mRNA levels of *vha-5, vha-10, vha-13*, and *vha-19,* as well as transcription factors *hlh-30*/TFEB and *daf-16*/FOXO were increased approximately 2-fold in *mir-1* mutants compared to age-matched wild-type worms (Figure 3A), consistent with the idea that these genes are miR-1 targets.

To investigate whether miR-1 also regulates candidates at protein level, we endogenously tagged the v-ATPase subunits *vha-5, vha-10, vha-13* and *vha-19* by CRISPR/Cas9 using an N-terminal 3xFlag-mNeonGreen-tag. Tagging *vha-19* and *vha-10* caused lethality and were not pursued further. Tagged *vha-5* showed significant upregulation in the pharynx in *mir-1* mutants compared to wild-type, but not in vulva muscle (Supplementary Figure 3A and B, Supplemental Table 7). Furthermore, RNAi knockdown only weakly suppressed *mir-1* motility (Figure 2E-G, Supplemental Table S2). N-terminally tagged *vha-13(syb586),* however, was viable, showed expression that was regulated, and harboured two potential *mir-1* binding sites in the 3' UTR (Figure 3F, Supplemental Figure 3C). Moreover, *vha-13* RNAi (*vha-13i)* significantly compromised the motility of *mir-1*;Q35 strains in the RNAi screens (Figure 2C), which we further confirmed through thrashing assays and the circle test (Figure 2E-G). *vha-13i* also significantly reduced pharyngeal pumping and life span in the *mir-1*;Q35 background compared to *luci* RNAi controls (Figures 2H and I, Supplemental Tables 1 and 2), yet had relatively minor effects on the motility of N2;Q35 itself (Supplemental Figure 2F). We therefore focused on *vha-13* as a promising candidate to pursue in depth for regulatory interactions with miR-1.

We first characterized the expression pattern of *3xFlag::mNeonGreen::vha-13(syb586)* in more detail. The fusion protein was strongly expressed in the excretory cell, canal, hypodermis, as well as gut (Figure 3B). In the hypodermis *3xFlag::mNeonGreen::VHA-13* was localized in discrete foci (Figure 3B, Supplemental Figure 3D). Notably, *3xFlag::mNeonGreen::VHA-13* also resided in miR-1 expressing tissues of body wall muscle, sex muscles and pharynx, where it was more weakly expressed. Within muscle cells, VHA-13 localized to dense bodies (analogous to vertebrate Z disks) and intervening cytosol (Figure 3B, Supplemental Figure 3D).

Because *mir-1* is expressed in muscle tissues, we focused on quantifying the expression of *vha-13* in these tissues. Strikingly, we observed that *VHA-13* levels were upregulated in the pharyngeal isthmus of *mir-1* mutants (Figure 3C and D, Supplemental Table 7), while conversely, overexpression of the *mir-1* transgene decreased levels in this tissue relative to wild-type (Figure 3E, Supplemental Table 7). To further investigate whether miR-1 directly regulates *vha-13*, we altered two predicted miR-1 binding sites (BS) in the 3'UTR (Figure 3F). We first mutated miR-1 binding site 1 (*vha-13* BS1 *(syb504)*, at position 188-195 of *vha-13* 3'UTR), and then additionally miR-1 binding site 2 (*vha-13* BS2 *(syb2180)*, at position 253-58 of *vha-13* 3'UTR) in the endogenously-tagged *vha-13(syb586)* strain. When only BS1 was mutated, we still saw residual regulation of VHA-13 by miR-1 (Supplemental Figure 3E, Supplemental Table 7). Mutating both miR-1 binding sites (BS1,2: MUT2), however, de-repressed VHA-13 levels in the isthmus in the WT background (Figure 3G). In double mutants containing both *mir-1* and *vha-13* BS1,2 mutations, no clear regulation of *vha-13* expression was observed compared to the BS1,2 mutations alone (Figure 3G), suggesting that miR-1 modulates pharyngeal *vha-13* expression through both potential miR-1 BS sites.

We next sought to characterize *vha-13* regulation in the body wall muscle. However, it was not possible to accurately measure expression in this tissue using the *3xFlag::mNeonGreen::vha-13* strain due to the high expression levels in the adjacent hypodermis and gut. We therefore generated transgenic worms expressing flag-tagged *vha-13* containing its endogenous 3´UTR *(3xFlag::vha-13::vha-13* 3´UTR) under control of the muscle-specific *myo-3* promoter. Consistent with results seen in pharyngeal muscle, *vha-13* protein levels in the body wall muscle were also upregulated in *mir-1* mutants compared to WT, as measured by Western blots (Figure 3H and I). Exchanging the *vha-13* 3´UTR with the *unc-54* 3'UTR lacking miR-1 binding sites (*vha-13::unc-54 3´UTR*) blunted regulation by miR-1 (Figure 3H and I), indicating that *vha-13* is repressed by miR-1 via its 3'UTR in both body wall and pharyngeal muscle.

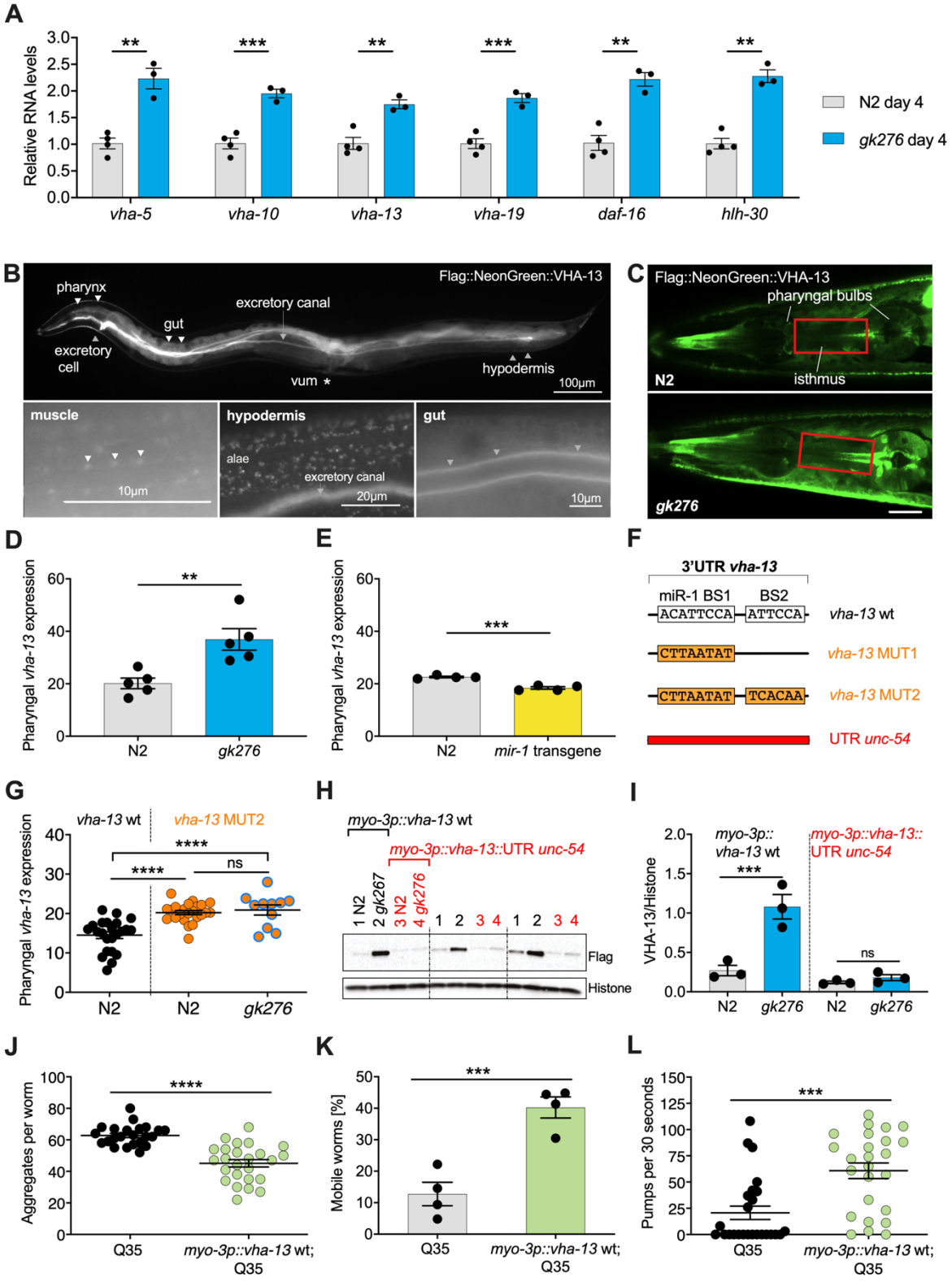


**Figure 3. miR-1 directly regulates *vha-13* via its 3'UTR in muscle tissue.**

**(A)** RT-qPCR of *vha-5, vha-10, vha-13* and *vha-19*, as well as *daf-16* and *hlh-30* mRNA levels in WT (N2) and *mir-1(gk276)* mutants on day 4 of adulthood. Mean ± SEM, N=3, one way ANOVA, **, p<0.01, ***, p<0.001.

**(B)** Expression pattern of endogenously tagged *3xFlag::mNeonGreen::vha-13* in pharynx, excretory cell and canal, gut, vulva muscle (vum), hypodermis, muscle (arrowhead indicates dense body).

**(C)** Confocal images of the head region in worms carrying endogenously tagged *3xFlag::mNeonGreen::vha-13* in late L4 *mir-1* and WT animals at 25°C. Red rectangle highlights the area of *vha-13* expression in the isthmus used for determination of mNeonGreen intensity. **(D)** Quantification of fluorescent intensity of *3xFlag::mNeonGreen::vha-13* expression in the isthmus of indicated genotypes (as shown in **(C)**) in late L4 larvae at 25°C. Mean ± SEM of N=5, t-test, **, p<0.01. **(E)** Quantification of fluorescent intensity of *3xFlag::mNeonGreen::vha-13* expression in the isthmus of N2; *mir-1* transgenic overexpression strain in late L4 larvae at 25°C. Transgenic worms (*mir-1* transgene) were compared to non-transgenic segregants (N2) of the same strain. Mean ± SEM of N=4, t-test, ***, p<0.001.

**(F)** Graphic showing the 3'UTR of endogenously tagged *3xFlag::mNeonGreen::vha-13. vha-13 wt: vha-13* wild-type 3´UTR. *vha-13* MUT1: one miR-1 binding site (BS) is mutated. *vha-13* MUT2: both miR-1 BSs are mutated. *unc-54*: the *vha-13* 3'UTR is substituted by *unc-54* 3'UTR. Nucleotide sequence of mutated miR-1 binding sites are shown below WT.

**(G)** Quantification of fluorescence intensity in the isthmus of L4 larvae with endogenously tagged *3xFlag::mNeonGreen::vha-13 vha-13 MUT2* 3'UTR in relation to *vha-13 wt* 3'UTR, in N2 and *mir-1(gk276)* mutant backgrounds at 25°C, using confocal imaging. Mean ± SEM of N=3, one representative experiment, one-way ANOVA, ****, p<0.0001, ns not significant.

**(H)** Western blot image of late L4 WT and *mir-1* mutants expressing transgenic flag-tagged *vha-13* in body wall muscle (*myo-3p*::*vha-13*) with either the *unc-54* 3´UTR (labelled in red), which lacks miR-1 BSs, or the wt *vha-13* 3´UTR which contains the two miR-1 BSs (labelled in black), immunoblotted with anti-Flag and anti-Histone H3 antibodies. Histone H3 loading control is shown below. Biological replicates (N=3) separated by dashed lines. **(I)** Quantification of Western blot shown in **(H)**, with flag-tag intensity normalized to histone H3 loading control, mean ± SEM of N=3, one-way ANOVA, ***, p<0.001, ns, not significant.

**(J)** Quantification of aggregates in Q35 worms expressing transgenic *vha-13* in the body wall muscle (*myo-3p*::*vha-13*;Q35) or non-transgenic segregants (Q35) of the same strain. 25 worms per genotype, mean ± SEM of one representative experiment, N=4, t-test, ***, p<0.001.

**(K)** Motility of Q35 worms expressing transgenic *vha-13* in the body wall muscle (*myo-3p*::*vha-13*;Q35) or non-transgenic segregants (Q35) of the same strain in circle test. Mean ± SEM. One experiment of N=2, t-test, ***, p<0.001.

**(L)** Pharyngeal pumping rate of *myo-3p*::*vha-13*;Q35 and Q35 non-transgenic segregants of the same strain. One representative experiment of N=4, mean ± SEM, t-test, ***, p<0.001.

Since *mir-1* mutation resulted in *vha-13* upregulation, we asked whether *vha-13* overexpression was sufficient to yield phenotypes similar to *mir-1* mutants. In accord with this idea, overexpressing *vha-13* in the muscle of Q35 worms significantly reduced aggregate number, improved motility, and enhanced pharyngeal pumping ability (Figure 3J-L, Supplemental Figure 3F, Supplemental Table 2). It also significantly increased the life span of Q35 animals compared to non-transgenic controls in 2/4 experiments (Supplemental Figure G, Supplemental Table 1). Altogether these data

suggest that miR-1 and VHA-13 work in the same regulatory pathway to influence muscle physiology.

**miR-1 regulates *hlh-30*/TFEB transcription factor**

Our RT-PCR experiments indicated that miR-1 also regulates mRNA levels *hlh-30/TFEB* and *daf-16*/FOXO transcription factors (Figure 3A). These factors modestly affected motility in the circle test (Figure 2F), and we wondered if regulation extended to the protein level. When we examined endogenously tagged *hlh-30*, we saw no obvious regulation of protein expression levels when measured by fluorescence intensity in the pharynx (Supplemental Figure 4A and B, Supplemental Table 7). Surprisingly, however, we observed that nuclear localization of HLH-30::mNeonGreen in the hypodermis of day 4 adults grown at 25°C was significantly increased in the *mir-1* background (Figure 4A and 4B). This finding suggests that miR-1, either directly or indirectly, regulates HLH-30 in distal tissues.

**miR-1 affects lysosomal biogenesis**

As the v-ATPase is an integral component of the lysosome, we asked wether miR-1 generally affects lysosomal structure and function. To test this idea, we first used a *lmp-1p::lmp-1::gfp* reporter strain. LMP-1 protein localizes to the membrane of lysosomes and is a marker for lysosomal biogenesis (Hermann et al., 2005). LMP-1 protein levels were significantly increased in *mir-1* mutants compared to WT control, as measured by Western blot analysis (Figure 4C and D). The v-ATPase hydrolyses ATP to pump protons across the membrane, resulting in acidification of the lysosome lumen (Beyenbach & Wieczorek, 2006). We therefore asked whether *mir-1* mutants affect the number of acidified lysosomes. Using Lysotracker Red, a dye that targets acidic membranous structures such as lysosomes (Chazotte, 2011), we observed an increase in the number of acidified puncta in *mir-1* mutants at day 4 of adulthood (Figure 4E and F). Due to technical limitations, lysotracker staining could only be observed in the worm intestine. This result leaves open the question as to whether lysosomes are also regulated in the muscle and whether *mir-1*, being expressed in muscle tissue, might have a cell non-autonomous effect. Nonetheless, the overall increase in lysosome biogenesis is consistent with the upregulation of lysosomal

components, such as the v-ATPase subunits, and a possible cause of miR-1-dependent regulation of proteostasis.

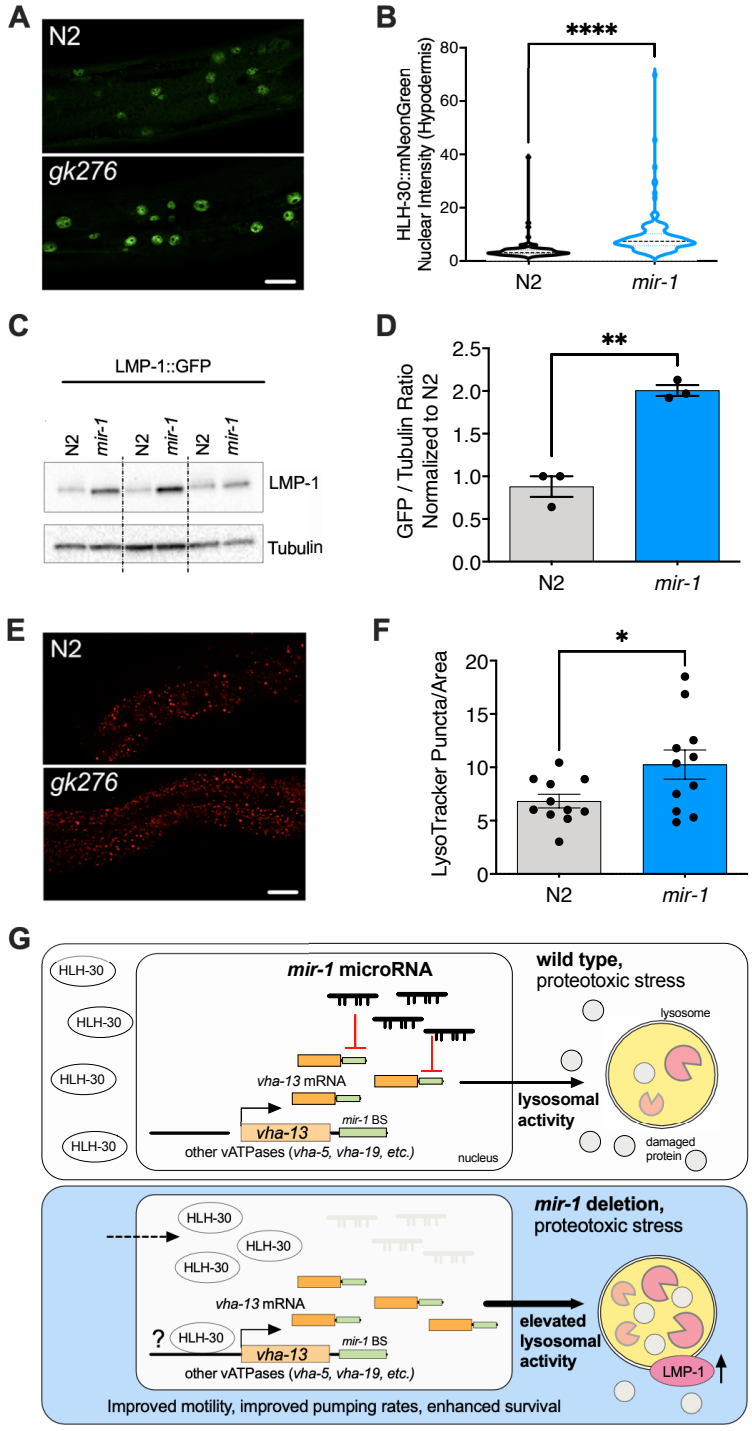


**Figure 4. *mir-1* mutation enhances lysosomal biogenesis and acidification.**

**(A)** Fluorescent image comparing HLH-30::mNeonGreen nuclear localization in the hypodermis of the *mir-1(gk276)* and WT (N2) backgrounds. **(B)** Quantitation of nuclear localization in (A). Violin plot, mean ± SEM of one representative experiment of N=3, t-test, ****, p<0.0001.

**(C)** Western blot of LMP-1::GFP in WT and *mir-1* mutants at the L4 stage, immunoblotted with anti-GFP or anti-α-tubulin antibodies. Biological replicates (N=3) separated by dashed lines. **(D)** Quantification of

the Western blot in **(C),** normalized to α-tubulin loading control. N=3 BR, line and error bars indicate mean ± SEM, t-test, **, p<0.01.
**(E)** Representative images of lysotracker staining in WT and *mir-1* mutants at day 4 of adulthood at 25°C. **(F)** Quantification of lysotracker images using a predefined squared area approximately spanning the second to fourth gut cell. Quantification was performed using Image J. N=3 BR, line and error bars indicate mean ± SEM of combined experiments, t-test, *, p<0.05.
**(G)** Working model. miR-1 normally limits proteoprotective pathways, downregulating the expression of *vha-13,* other v-ATPases and factors by binding miR-1 binding site(s) in the 3'UTR (miR-1 BS) of the corresponding mRNA (WT, proteotoxic stress). Loss of miR-1 under proteotoxic conditions results in free *vha-13* mRNA, higher VAH-13 protein levels, and elevated lysosomal activity (LMP-1). Nuclear localization of HLH-30/TFEB, a master regulator of lysosome biogenesis is also enhanced, collectively resulting in improved mid-life muscle motility, pharyngeal pumping, and organismal longevity under proteotoxic stress conditions.

## Discussion

Striated muscle is one of the most highly ordered tissues in the body, with molecular components organized in a lattice of contractile elements and attachments. This molecular apparatus is exposed to high energy and force during contraction, inflicting molecular damage requiring constant repair. Further, muscle is subject to growth, metabolic, and stress signalling pathways as well as neural inputs that also promote remodelling. Underlying muscle plasticity is the fine-tuned control of proteostasis, including protein synthesis, folding, trafficking and turnover, which must be precisely orchestrated to maintain muscle structure and function (Demontis et al., 2013). A decline in these processes during aging leads to diminished muscle performance and frailty, yet it remains elusive how various aspects of muscle proteostasis are coordinated.

In this work, we discovered that the muscle enriched microRNA miR-1 plays an important role in regulating muscle homeostasis via vacuolar ATPase function. Loss of *mir-1* ameliorates age-related decline in motility induced by models of aggregate-prone polyQ35. By inference, *mir-1* normally limits proteoprotective pathways. Computational and proteomic screens identified v-ATPase subunits as highly enriched targets of miR-1 regulation, suggestive of coordinate regulation, and whose downregulation reduced proteoprotection. Expression studies confirmed that several subunits (*e.g.*, *vha-5, vha-10, vha-13, vha-19*) showed miR-1 dependent regulation. In

particular, we demonstrated that *vha-13* expression is downregulated by miR-1 in muscle tissues via two distinct binding sites in its 3'UTR. Moreover, VHA-13 links miR-1 with muscle homeostasis, since *vha-13* downregulation abolished the improved mid-life motility, pharyngeal pumping and life span of *mir-1*;Q35 strains, while *vha-13* overexpression was sufficient to enhance these properties, similar to *mir-1* mutation. In accord with our findings, immunoprecipitation and sequencing of microRNA complexes revealed a number of v-ATPase subunit mRNAs, including *vha-13*, *vha-4, vha-10,* and *vha-17* as physically associated with *C. elegans* miR-1 (Grosswendt et al., 2014). Interestingly, mammalian homolog of VHA-13, ATP6V1A, as well as several other v-ATPase subunits (Stark, Brennecke, Bushati, Russell, & Cohen, 2005), harbour predicted miR-1 binding sites, suggesting that this regulatory module could be conserved in evolution.

The v-ATPase is a multisubunit enzyme which acidifies the endolysosomal lumen to control a plethora of cellular activities. Acidification regulates protein trafficking, endocytic recycling, synaptic vesicle loading, and autophagy, as well as the activity of multiple acid hydrolases and nutrient and ion transporters. Moreover, the v-ATPase itself serves as a docking site for regulating mTOR and AMPK complexes and affects metabolism (Settembre, Fraldi, Medina, & Ballabio, 2013; Zhang et al., 2014). Our studies highlight the importance of v-ATPase activity to muscle performance. A handful of studies ascribe a role for the v-ATPase in muscle. In mammalian cardiomyocytes, lipid loading inhibits the v-ATPase, leading to a decline in contractile function that could contribute to muscle deficits in diabetes (Wang et al., 2020). Lesions in VMA21 that disrupt v-ATPase assembly have also been shown to cause myopathies (Dowling, Moore, Kalimo, & Minassian, 2015). Conceivably the v-ATPase could play an important role in protein turnover and remodeling of muscle structure but could also impact muscle homeostasis through metabolic wiring or protein trafficking.

Surprisingly we also found that some *mir-1* phenotypes were not strictly limited to muscle, since we observed a global increase in levels of lysosomal LMP-1::GFP in Western blots, increased lysosomal acidification in the intestine, as well as enhanced nuclear localization of HLH-30/TFEB in the hypodermis. Given that *mir-1* is muscle-expressed, this observation could suggest cell non-autonomous regulation of lysosomal biogenesis and associated activities by *mir-1*, acting either directly or indirectly. Conceivably, miR-1 is secreted from muscle to affect physiology in other

tissues. In mammals miR-1 has been identified as a circulating microRNA found in serum exosomes upon exercise stress or cardiac infarction, suggesting it could act systemically (Cheng et al., 2019) (D'Souza et al., 2018). In this light, it is intriguing that the v-ATPase itself is implicated in exosomal activity activity (Liegeois, Benedetto, Garnier, Schwab, & Labouesse, 2006). Alternately, *mir-1* could act indirectly through production of a myokine that affects distal tissues.

miR-1 has been implicated in regulating a number of targets and physiologic processes. In mammals, miR-1 and its homolog miR-133 are essential to cardiac development and function, where they have been shown to regulate Notch ligand Dll-1, the GTPase dynamin 2 (DNM2), FZD7 (Frizzled-7), and FRS2 (fibroblast growth factor receptor substrate 2) as targets (Ivey et al., 2008; Liu et al., 2011; Mitchelson & Qin, 2015). Surprisingly knockout of mammalian *mir1/mir133* specifically in muscle has little overt effect on muscle structure, but rather regulates the developmental transition from glycolytic to oxidative metabolism via the MEF-2/Dlk1-Dio3 axis, affecting running endurance (Wust et al., 2018). Similarly, *C. elegans* miR-1 regulates *mef-2*, in this case affecting retrograde signalling at the neuromuscular junction (Simon et al., 2008). We also observed that animals lacking *mir-1* have little overt change in muscle structure or function alone, though we saw upregulation of a number of muscle proteins and downregulation of mitochondrial proteins in our proteomic analysis. Indeed, most microRNA knockouts do not lead to observable phenotypes in *C. elegans* (Miska et al., 2007), suggesting that microRNAs often work redundantly or in response to stress to fine tune gene expression.

Recently Pocock and colleagues reported that miR-1 downregulates the rab GTPAse TBC-7/TBC1D15, thereby promoting autophagic flux in worms and human cells (Nehammer et al., 2019). In *C. elegans* they observed that *mir-1(+)* ameliorates polyQ40 proteotoxicity, seemingly contradicting our results. Other studies suggest that mammalian *mir-1* can either promote or inhibit autophagy, dependent on context (Ejlerskov, Rubinsztein, & Pocock, 2020; Hua, Zhu, & Wei, 2018; Xu, Cao, Zhang, Zhang, & Yue, 2020). Whether miR-1 is proteoprotective or limits proteoprotection in *C. elegans* could hinge on many factors. We used polyQ35, Pocock et al used polyQ40; these species differ in the effect on aggregation and motility (Morley et al., 2002). For motility assays, we assessed all animals that were alive, they excluded paralyzed animals. We performed motility assays on day 8, they performed them

earlier in adulthood. Because microRNAs generally fine tune regulation, and often work in feedback circuits, their impact on physiology can be subtle, and small differences in culture conditions, genetic background, assay method, or metabolic state could give rise to divergent outcomes.

Among the putative miR-1 targets that we identified in *C. elegans* are the pro-longevity transcription factors DAF-16/FOXO and HLH-30/TFEB, which regulate lysosome biogenesis, proteostasis, and metabolism, and act in insulin/IGF and mTOR signalling pathways (Lin et al., 2018; O'Rourke & Ruvkun, 2013; Settembre et al., 2011). *mir-1* mutation led to an upregulation of their mRNA during adulthood and enhanced nuclear localization of HLH-30. Further RNAi knockdown of these factors modestly diminished the motility improvement of *mir-1* mutants in the circle test, consistent with roles in a miR-1 signalling pathway. Whether these transcription factors are direct targets of miR-1 regulation remains to be seen. Notably, miR-1 predicted targets also include pro-ageing components of mTOR signalling such as *let-363/*mTOR and *raga-1/*RagA (targetscan.org), which also regulate the activity of these transcription factors. Hence the balance or timing of pro- and anti-ageing factors could also differentially influence the physiologic phenotype at a systemic level. Interestingly, VHA-13/ATP6VIA subunit has been shown to regulate mTOR lysosomal recruitment and activity (Chung et al., 2019) and mTOR signalling regulates the activity of TFEB at the lysosomal surface (Settembre et al., 2013). Upregulation of v-ATPase activity is also associated with the clearance of oxidized protein and rejuvenation of the *C. elegans* germline (Bohnert & Kenyon, 2017). Thus, in the future it will be interesting to further unravel the miR-1 molecular circuitry surrounding lysosomal function and proteostasis, and see whether miR-1 similarly regulates v-ATPase function in humans.

## Materials and Methods

### *C. elegans* strains and culture

*C. elegans* strains were maintained at 20°C on nematode growth medium (NGM) plates seeded with a lawn of *E. coli* strain OP50, unless noted otherwise.

N2 Bristol (wild-type) CGC

AA2508, *mir-1(gk276)* I

AA4575, *mir-1(dh1111)* I

AM140, *rmIs132[unc-54p::Q35::YFP]* I

AA4403, *mir-1(gk276); rmIs132[unc-54p::Q35::YFP]* I

AA4577, *mir-1(dh1111) rmIs132[unc-54p::Q35::YFP*] I

AA3275, *N2; dhEx965[mir-1p::mir-1, myo-2p::mCherry]*

AA4810, *mir-1(gk276)* I*; rmIs132[unc-54p::Q35::YFP]; dhEx965[mir-1p::mir-1, myo-2p::mCherry]*

AA4865, N2; *dhEx1206[myo3p::flag::HA::mCherry::vha-13cDNA::unc-54* 3'UTR*, myo-2p::GFP]*

AA4866*, mir-1(gk276)* I*; dhEx1206[myo-3p::flag::HA::mCherry::vha-13cDNA::unc-54* 3'UTR*, myo-2p::GFP]*

AA5067, N2; dh*Ex1207[myo-3p::flag::HA::mCherry::vha-13cDNA::vha-13 3'UTR, myo-2p::GFP]*

AA5068, *mir-1(gk276)* I*; dhEx1207[myo-3p::flag::HA::mCherry::vha-13cDNA::vha-13 3'UTR, myo-2p::GFP]*

PHX586, *vha-13(syb586[3xFlag::mNeonGreen::vha-13])* V

AA4813, *mir-1(gk276)* I; *vha-13(syb586[3xFlag::mNeonGreen::vha-13])* V

AA4850, *vha-13(syb586[3xFlag::mNeonGreen::vha-13])* V; *dhEx965[mir-1p::mir-1, myo-2p::mCherry]*

PHX587, *vha-13(syb587,syb504[3xFlag::mNeonGreen::vha-13* miR-1 BS1 mutated*])* V. Also named in the text *vha-13* MUT1.

AA4184, *mir-1(gk276)* I; *vha-13(syb587,syb504[3xFlag::mNeonGreen::vha-13* miR-1 BS1 mutated*])* V

PHX2180, *vha-13(syb2180,syb587,syb504[3xFlag::mNeonGreen::vha-13* miR-1 BS1,2 mutated*])* V. Also named in the text *vha-13* MUT2.

AA5123, *mir-1(gk276)* I; *vha-13(syb2180,syb587,syb504[3xFlag::mNeonGreen::vha-13* miR-1 BS,2 mutated*])* V

PHX1093, *vha-5(syb1093[3xFlag::mNeonGreen::vha-5])* IV

AA5069, *mir-1(gk276)* I; *vha-5(syb1093[3xFlag::mNeonGreen::vha-5])* IV

PHX809, *hlh-30(syb809[hlh-30::mNeonGreen])* IV

AA5195, *mir-1(gk276)* I; *hlh-30(syb809[hlh-30::mNeonGreen])* IV

**Molecular cloning**

All restriction digest reactions were performed with enzymes provided by NEB according to the user's manual. T4 DNA Ligase (NEB) was used for ligation reactions. Chemically competent DH5α *Escherichia coli* (LifeTechnologies) was used for transformation following the manufacturer's instructions. QIAprep Miniprep or Midiprep Kits (Qiagen) were used for plasmid purification. Cloning was verified by PCR followed by gel electrophoresis and sequencing.

To make the rescuing *mir-1* transgene, primer pair "celmir1fwd2/rvs2" (Table S8) was used to insert the *mir-1* coding region into vector L3781 downstream of *gfp*. The *mir-1* promoter was then cloned 5' to *gfp* using the primer pair "m1p fwd/rvs"(Table S8). To make muscle expressed *vha-13* constructs, the *vha-13* cDNA was amplified with Kpn1 overhangs using primers vha-13 fwd/rvs (Table S8) and cloned into vector pDESTR4-R3 to give *myo3p::flag::HA::mCherry::vha-13cDNA::unc-54* 3'UTR. The *unc-54* 3'UTR was excised with Not1/BglI and replaced with the *vha-13* 3'UTR using primers vha-13U fwd/rvs (Table S8) to generate *myo3p::flag::HA::mCherry::vha-13cDNA::vha-13 3'UTR.*

**Generation of transgenic worm strains**

Transgenic worms containing extrachromosomal arrays were generated by microinjection. To generate the ***myo3p::flag::HA::mCherry::vha-13cDNA::unc-54* 3'UTR** strain, a mix of *myo3p::flag::HA::mCherry::vha-13cDNA::unc-54* 3'UTR DNA (40ng/ µl), *myo-2p::gfp* co-transformation marker (5 ng/ µl plasmid pPD122.11) and fill DNA (TOPO empty vector, 55 ng/ µl ) was injected into young N2 adults using an Axio Imager Z1 microscope (Zeiss) with a manual micromanipulator (Narishige) connected to a microinjector (FemtoJet 4x, Eppendorf). We obtained the strain AA4865: N2*; dhEx1206[myo3p::flag::HA::mCherry::vha-13cDNA::unc-54 3'UTR, myo-2p::gfp]*, which was then used to cross the transgene into other genetic backgrounds.

A similar strategy was used to create AA5067, N2; dh*Ex1207[myo3p::flag::HA::mCherry::vha-13cDNA::vha-13 3'UTR, myo-2p::GFP].*

The ***mir-1* transgene** strain was generated by injection mix containing *mir-1p::mir-1* plasmid, *myo-2p::mCherry* co-transformation marker (5 ng/ µl plasmid pPD122.11) and fill DNA (L3781 empty vector). The resultant strain AA3275 (*N2; dhEx965[mir-1p::mir-1, myo-2p::mCherry]*) was then used to cross the *dhEx965* transgene to *mir-1(gk276); rmIs132[p(unc-54) Q35::YFP]* to give *mir-1(gk276); rmIs132[p(unc-54) Q35::YFP]; dhEx965[mir-1p::mir-1, myo-2p::mCherry]*, AA4810. For transgenic worm strains, non-transgenic worms of the same strain were used as controls.

The ***mir-1* deletion allele *dh1111*** was generated using CRISPR/Cas9 mutagenesis. We designed CRISPR guides using the EnGen sgRNA Designer (https://sgrna.neb.com/#!/sgrna), synthesized guides with the Engen sgRNA synthesis kit and analysed them by gel electrophoresis and tape station. We injected worms with an injection mix containing Cas9 EnGen (NEB), 4 sgRNAs against *mir-1* (AAGAAGTATGTAGAACGGGG, GTAAAGAAGTATGTAGAACG, TATAGAGTAGAATTGAATCT, ATATAGAGTAGAATTGAATC), one sgRNA against *dpy-10* (CGCTACCATAGGCACCACG), KCl, Hepes pH 7.4 and water. Prior to injection we incubated the mixture for 10 minutes at 37°C to allow activation of Cas9. Following injection, we singled out worms with Dpy phenotype in the F1 generation and genotyped them for *mir-1* deletion using *mir-1* genotyping primers (Supplemental Table 8). We sequenced the PCR products of candidate worms with Sanger sequencing and verified that the deletions resulted in loss of *mir-1* expression using Taqman-based quantification of mature miRNA levels.

**Endogenous fluorescently tagged strains** were generated by tagging *vha-5* or *vha-13* with 3xFLAG-mNeonGreen tag at the N-terminus using CRISPR–Cas9 (SunyBiotech). The *vha-13* 3'UTR mutants BS1 and BS2 were generated using CRISPR–Cas9, by further mutating one or both putative miR-1 binding sites in the 3'UTR of the endogenous FLAG-mNeonGreen-tagged *vha-13 gene* (SunyBiotech). PHX809 *hlh-30::mNeonGreen* endogenously tagged *hlh-30* was generated by placing *mNeonGreen* at the C-terminus using CRISPR–Cas9 (SunyBiotech).

669 **Determination of progeny number**

670 Single worms were maintained on an NGM agar plate and transferred every day
671 until the reproductive period was complete. The number of F1 progeny per individual
672 worm was counted at the L4 or young adult stage. Experiments were repeated at least
673 three times.

674 **Quantitation of polyQ aggregates**

675 Whole-worm images of day 4 adults were taken with an Axiocam 506 mono
676 (Zeiss) camera using the 5x objective of a Zeiss Axio Imager Z1 microscope (20ms
677 exposure). Q35 aggregate numbers were evaluated from photos at 163%
678 magnification. Genotypes of the samples were blinded during the counting. Aggregates
679 were defined as discrete structures or puncta above background.
680
681 **Motility, thrashing and pumping behaviour**

682 To analyse worm motility by the circle test, 20 to 25 worms were placed in the
683 centre of a 6 cm agar plate with bacteria, marked with 1 cm circle on the bottom. After
684 a defined time period (1 or 30 minutes) the number of worms that left the circle were
685 counted. To determine thrashing rate, individual worms were transferred to M9 buffer
686 and the number of body bends in a 20 to 30 second interval was scored. Pharyngeal
687 pumping rates were measured by counting grinder contraction in the terminal bulb over
688 20 to 30 seconds. Genotypes were blinded during all experiments.
689
690 **CeleST Assay**

691 The *C. elegans* Swim Test (CeleST) assay was used to assess animal motility
692 while swimming; assays were conducted as described previously (Ibanez-Ventoso,
693 Herrera, Chen, Motto, & Driscoll, 2016; Restif et al., 2014). Four or five animals were
694 picked and placed into the swimming arena, which was a 50 µl aliquot of M9 Buffer
695 inside a 10 mm pre-printed ring on the surface of a glass microscope slide (Thermo
696 Fisher Scientific). Images of the animals within the swim arena were acquired with a
697 LEICA MDG41 microscope at 1x magnification with a Leica DFC3000G camera. Image
698 sequences of 30 seconds in duration were captured at a rate of ~16 frames per second.
699 The established CeleST software was used to process the image sequences and
700 extract 8 measures that are descriptive of *C. elegans* swim motility. As not all images
701 in a sequence are always successfully processed by the CeleST software, animals for
702 which fewer than 80% of frames were valid were excluded from the analysis. For each

703 measure, single measurements that did not fit within the range of normally observed
704 values were deemed outliers and also excluded from the analysis. Unpaired Student's
705 t-test was used to test for statistical significance between two strains at adult day 4 and
706 day 8.
707
708 **Life span and heat stress experiments**
709 Life span experiments were performed as described (Gerisch et al., 2007). Day
710 0 corresponds to the L4 stage. Life spans were determined by scoring a population of
711 100 to 120 worms per genotype every day or every other day. Worms that exploded,
712 had internal hatch or left the plate were censored. Heat stress experiments were
713 performed at 35°C (Gerisch et al., 2007). Day 1 adult worms were transferred onto pre-
714 heated (35°C) plates 6 cm plates seeded with OP50. Worms were kept at 35°C and
715 scored every hour for live versus dead. Experiments were repeated at least three
716 times. Data were analysed with Microsoft Excel 16.12 and GraphPad Prism 7
717 Software. *P*-values were calculated using the Log-rank (Mantel-Cox) test to compare
718 two independent populations.
719
720 **RNAi Treatment**
721 Worms were grown from L4 onwards unless mentioned otherwise on *E. coli*
722 HT115 (DE3) bacteria expressing dsRNA of the target gene under the control of an
723 IPTG-inducible promotor. RNAi colonies were grown overnight at 37°C in Luria Broth
724 with 50 µg/ml Ampicillin and 10 µg/ml tetracycline. The cultures were spun down at
725 4,000 rpm at 4°C for 10 minutes. 500 µl of one-fold concentrated culture was seeded
726 onto NGM plates containing 1 M isopropyl β-D-1-thiogalactopyranoside (IPTG) to
727 induce dsRNA expression. RNAi clones were selected from the Ahringer or Vidal
728 library (Kamath & Ahringer, 2003; Rual et al., 2004). Clone identity was confirmed by
729 sequencing. Bacteria containing luciferase were used as control.
730
731 **RNAi screen for *mir-1* suppressors**
732 *mir-1(gk276)* Q35 worms were grown from L4 on RNAi of the candidates
733 identified in the bioinformatic or proteomic screen. Worms were maintained in the
734 presence of FUDR till day 8 of adulthood. The circle test was performed as described
735 above. The number of worms that left the circle was determined after 1 minute.
736 Selected candidates identified in the circle test were examined in the body bending
737 assay (see above). The effect of selected candidate RNAi clones was additionally

738 tested on polyQ35 in the wild-type background as counter screen. For this experiment
739 worms were grown till day 5 of adulthood. Motility assays were performed on day 5 of
740 adulthood because Q35 wild-type worms were less motile than the *mir-1(gk276)* Q35
741 and were largely paralyzed by day 8.
742
743 **RNA extraction and real-time qPCR analysis**
744 Worm populations (ca. 500 animals) were harvested on day 4 of adulthood and
745 washed twice in cold M9. Worm pellets were taken up in 700 µl QIAzol reagent
746 (Qiagen) and snap frozen in liquid nitrogen. Samples were subjected to 4 freeze/thaw
747 cycles and homogenized with 1.0 mm zirconia/silica beads (Fisher Scientific) in a
748 Tissue Lyser LT (Qiagen) for 15 min at full speed. After homogenization, 600µl
749 supernatant was transferred to fresh tubes and 120 µl chloroform were added to each
750 tube. Components were mixed by vortexing and incubated for 2 min at room
751 temperature. After 15 min centrifugation at 12,000 *g* 4°C, the aqueous phase was
752 collected for total RNA extraction using the RNeasy or miRNeasy Mini Kit (Qiagen)
753 according to manufacturer's instructions. RNA quantity and quality were determined
754 on a NanoDrop 2000c (PeqLab) and cDNA was prepared using the iScript cDNA
755 Synthesis Kit (BioRad). To quantify RNA expression, we used the Power SYBR Green
756 Master Mix (Applied Biosystems) on a ViiA 7 Real-Time PCR system (Applied
757 Biosystems). Four technical replicates were pipetted on a 384-well plate using the
758 JANUS automated workstation (PerkinElmer). Expression of target RNA was
759 calculated from comparative CT values, normalized to *ama-1* or *cdc-42* as internal
760 controls using the corresponding ViiA7 software. All unpublished primers were
761 validated by determination of their standard curves and melting properties. For
762 quantification of *mir-1* we used Taqman probes from LifeTechnologies/ThermoFisher
763 Scientific (Assay ID 000385) and normalized to expression of U18 as measured by
764 Taqman probes from LifeTechnologies/ThermoFisher Scientific (Assay ID 001764).
765 We used N=4 independent biological replicates, and four technical replicates for every
766 biological sample (for primers, refer to Supplementary Table 8).
767
768 **Western blot analysis**
769 For Western blot analysis synchronized young adult or gravid day 1 adult worms
770 were picked into Eppendorf tubes containing M9, snap frozen in liquid nitrogen and
771 lysed in 4x SDS sample buffer (Thermo Fisher) containing 50 mM DTT. After boiling

and sonication, equal volumes were subjected to reducing SDS-PAGE and transferred to nitrocellulose membranes. The membranes were then blocked for two hours at room temperature in 5% milk in Tris-buffered Saline and Tween20 (TBST) and probed with the primary antibodies in TBST with 5% milk overnight at 4 °C. Specific secondary antibodies (mouse or rabbit) were used at a concentration of 1:5000 in TBST with 5% milk at room temperature for 2 hours. The membranes were developed with Western Lightening Plus- Enhanced Chemiluminescence Substrate (PerkinElmer). Bands were detected on a ChemiDoc MP Imaging System (BioRad) and the intensity quantified using the corresponding Image Lab software (BioRad). The following antibodies were used: anti-GFP (JL-8 Living Colors, mouse monoclonal), anti-Histone H3 (ab1791 Abcam, rabbit polyclonal), anti-α-Tubulin (T6199 Sigma, mouse monoclonal), anti-FLAG (F1804 Sigma, mouse monoclonal), anti-mouse IgG (G-21040 Invitrogen, goat polyclonal coupled with horseradish peroxidase), anti-rabbit IgG (G-21234 Invitrogen, goat polyclonal coupled with horseradish peroxidase).

**Proteomic analysis**

For **sample collection and preparation**, day 1 N2 and *mir-1(gk276)* worms were synchronized by egg laying, and $n \geq 5000$ worms per genotype were collected in M9. Samples were washed three times in M9 and directly frozen in liquid nitrogen and stored at –80 °C. 5 independent biological replicates of each genotype were collected for further analyses. For **protein extraction** samples were thawed and boiled in lysis buffer (100 mM Tris-HCl, 6 M guanidinium chloride, 10 mM Tris(2-carboxyethyl)phosphine hydrochloride, 40 mM 2-Chloroacetamide) for 10 min, lysed at high performance with a Bioruptor Plus sonicator (Diagenode) using 10 cycles of 30 s sonication intervals. The samples were then boiled again, centrifuged at 20000*g* for 20 min, and diluted 1:10 in 20 mM Tris pH 8.3 / 10% acetonitrile (ACN). Protein concentration was measured using BCA Protein Assays (Thermo Fisher). Samples were then digested overnight with rLys-C (Promega), the peptides were cleaned on a Supelco Visiprep SPE Vacuum Manifold (Sigma) using OASIS HLB Extraction cartridges (Waters). The columns were conditioned twice with Methanol, equilibrated twice with 0.1% formic acid, loaded with the sample, washed three times with 0.1% formic acid and the peptides eluted with 60% ACN / 0.1% formic acid. The samples were dried at 30°C for roughly 4 h in a Concentrator (Eppendorf) set for volatile aqueous substances. The dried peptides were taken up in 0.1% formic acid and the

806 samples were analysed by the Max Planck Proteomic Core facility. **Mass**
807 **spectrometry** data acquisition, computational proteomic analysis and differential
808 expression analysis were performed as described (Tharyan et al., 2020). Upon
809 inspection of the numbers of quantified proteins and the raw proteomic data, two
810 replicates of N2 were excluded from further analysis.
811
812 **Microscopy and expression analysis**
813 For confocal microscopy *vha-13*, *vha-5 and hlh-30* endogenously tagged with
814 mNeonGreen were synchronized via egg and maintained at 25°C to induce mild stress.
815 *hlh-30* worms were imaged as day 4 adults, while *vha-13* and *vha-5* worms as L4s,
816 because of high mNeonGreen background expression at day 4 adulthood. Worms
817 were anaesthetized with 40 µM sodium azide, mounted on slide with 2% agar pad and
818 imaged with a Leica TCS SP8 microscope equipped with HC PL APO CS2 63X/1.40
819 Oil and white light laser. Images were analysed using photoshop or Fiji software. To
820 quantitate acidic lysosomes, worms grown at 25°C were incubated 48 hours prior to
821 imaging with 2 µM LysoTracker Red DND-99 (Life Technologies). Worms were imaged
822 as day 4 adults as described above. Number of puncta in a predefined squared area
823 in the intestine (approximately spanning the second to fourth gut cell) were counted.
824
825 **Statistical Analysis**
826 The statistical tests performed in this study are indicated in figure legends and
827 in the method detail section. Data are represented as mean ± SEM or as individual
828 data points, as stated in the figure legends. Number of replicates and animals for each
829 experiment are enclosed in their respective figure legends.
830
831 **Data and Software Availability**
832 Accession Code: The mass spectrometry proteomics data have been
833 deposited to the ProteomeXchange Consortium via the PRIDE partner repository
834 (Perez-Riverol et al., 2019) with the dataset identifier PXD023544.
835

## References


Andachi, Y., & Kohara, Y. (2016). A whole-mount in situ hybridization method for microRNA detection in Caenorhabditis elegans. *RNA, 22*(7), 1099-1106. doi:10.1261/rna.054239.115

Betel, D., Wilson, M., Gabow, A., Marks, D. S., & Sander, C. (2008). The microRNA.org resource: targets and expression. *Nucleic Acids Res, 36*(Database issue), D149-153. doi:10.1093/nar/gkm995

Beyenbach, K. W., & Wieczorek, H. (2006). The V-type H+ ATPase: molecular structure and function, physiological roles and regulation. *J Exp Biol, 209*(Pt 4), 577-589. doi:10.1242/jeb.02014

Bohnert, K. A., & Kenyon, C. (2017). A lysosomal switch triggers proteostasis renewal in the immortal C. elegans germ lineage. *Nature, 551*(7682), 629-633. doi:10.1038/nature24620

Brignull, H. R., Morley, J. F., Garcia, S. M., & Morimoto, R. I. (2006). Modeling polyglutamine pathogenesis in C. elegans. *Methods Enzymol, 412*, 256-282. doi:10.1016/S0076-6879(06)12016-9

Cartee, G. D., Hepple, R. T., Bamman, M. M., & Zierath, J. R. (2016). Exercise Promotes Healthy Aging of Skeletal Muscle. *Cell Metab, 23*(6), 1034-1047. doi:10.1016/j.cmet.2016.05.007

Chazotte, B. (2011). Labeling lysosomes in live cells with LysoTracker. *Cold Spring Harb Protoc, 2011*(2), pdb prot5571. doi:10.1101/pdb.prot5571

Chen, X., Ba, Y., Ma, L., Cai, X., Yin, Y., Wang, K., . . . Zhang, C. Y. (2008). Characterization of microRNAs in serum: a novel class of biomarkers for diagnosis of cancer and other diseases. *Cell Res, 18*(10), 997-1006. doi:10.1038/cr.2008.282

Cheng, M., Yang, J., Zhao, X., Zhang, E., Zeng, Q., Yu, Y., . . . Qin, G. (2019). Circulating myocardial microRNAs from infarcted hearts are carried in exosomes and mobilise bone marrow progenitor cells. *Nat Commun, 10*(1), 959. doi:10.1038/s41467-019-08895-7

Chung, C. Y., Shin, H. R., Berdan, C. A., Ford, B., Ward, C. C., Olzmann, J. A., . . . Nomura, D. K. (2019). Covalent targeting of the vacuolar H(+)-ATPase activates autophagy via mTORC1 inhibition. *Nat Chem Biol, 15*(8), 776-785. doi:10.1038/s41589-019-0308-4

Cruz-Jentoft, A. J., Baeyens, J. P., Bauer, J. M., Boirie, Y., Cederholm, T., Landi, F., . . . European Working Group on Sarcopenia in Older, P. (2010). Sarcopenia: European consensus on definition and diagnosis: Report of the European Working Group on Sarcopenia in Older People. *Age Ageing, 39*(4), 412-423. doi:10.1093/ageing/afq034

D'Souza, R. F., Woodhead, J. S. T., Zeng, N., Blenkiron, C., Merry, T. L., Cameron-Smith, D., & Mitchell, C. J. (2018). Circulatory exosomal miRNA following intense exercise is unrelated to muscle and plasma miRNA abundances. *Am J Physiol Endocrinol Metab, 315*(4), E723-E733. doi:10.1152/ajpendo.00138.2018

Demontis, F., Piccirillo, R., Goldberg, A. L., & Perrimon, N. (2013). Mechanisms of skeletal muscle aging: insights from Drosophila and mammalian models. *Dis Model Mech, 6*(6), 1339-1352. doi:10.1242/dmm.012559

Distefano, G., & Goodpaster, B. H. (2018). Effects of Exercise and Aging on Skeletal Muscle. *Cold Spring Harb Perspect Med, 8*(3). doi:10.1101/cshperspect.a029785

Dowling, J. J., Moore, S. A., Kalimo, H., & Minassian, B. A. (2015). X-linked myopathy with excessive autophagy: a failure of self-eating. *Acta Neuropathol, 129*(3), 383-390. doi:10.1007/s00401-015-1393-4

884 Ejlerskov, P., Rubinsztein, D. C., & Pocock, R. (2020). IFNB/interferon-beta regulates
885 autophagy via a MIR1-TBC1D15-RAB7 pathway. *Autophagy, 16*(4), 767-769.
886 doi:10.1080/15548627.2020.1718384
887 Gerisch, B., Rottiers, V., Li, D., Motola, D. L., Cummins, C. L., Lehrach, H., . . . Antebi, A.
888 (2007). A bile acid-like steroid modulates Caenorhabditis elegans lifespan through
889 nuclear receptor signaling. *Proc Natl Acad Sci U S A, 104*(12), 5014-5019.
890 doi:10.1073/pnas.0700847104
891 Grosswendt, S., Filipchyk, A., Manzano, M., Klironomos, F., Schilling, M., Herzog, M., . . .
892 Rajewsky, N. (2014). Unambiguous identification of miRNA:target site interactions by
893 different types of ligation reactions. *Mol Cell, 54*(6), 1042-1054.
894 doi:10.1016/j.molcel.2014.03.049
895 Gu, S., & Kay, M. A. (2010). How do miRNAs mediate translational repression? *Silence, 1*(1),
896 11. doi:10.1186/1758-907X-1-11
897 Guo, Z., Maki, M., Ding, R., Yang, Y., Zhang, B., & Xiong, L. (2014). Genome-wide survey of
898 tissue-specific microRNA and transcription factor regulatory networks in 12 tissues.
899 *Sci Rep, 4*, 5150. doi:10.1038/srep05150
900 Hermann, G. J., Schroeder, L. K., Hieb, C. A., Kershner, A. M., Rabbitts, B. M., Fonarev,
901 P., . . . Priess, J. R. (2005). Genetic analysis of lysosomal trafficking in
902 Caenorhabditis elegans. *Mol Biol Cell, 16*(7), 3273-3288. doi:10.1091/mbc.e05-01-
903 0060
904 Herndon, L. A., Schmeissner, P. J., Dudaronek, J. M., Brown, P. A., Listner, K. M., Sakano,
905 Y., . . . Driscoll, M. (2002). Stochastic and genetic factors influence tissue-specific
906 decline in ageing C. elegans. *Nature, 419*(6909), 808-814. doi:10.1038/nature01135
907 Hua, L., Zhu, G., & Wei, J. (2018). MicroRNA-1 overexpression increases chemosensitivity of
908 non-small cell lung cancer cells by inhibiting autophagy related 3-mediated
909 autophagy. *Cell Biol Int, 42*(9), 1240-1249. doi:10.1002/cbin.10995
910 Ibanez-Ventoso, C., Herrera, C., Chen, E., Motto, D., & Driscoll, M. (2016). Automated
911 Analysis of C. elegans Swim Behavior Using CeleST Software. *J Vis Exp*(118).
912 doi:10.3791/54359
913 Ivey, K. N., Muth, A., Arnold, J., King, F. W., Yeh, R. F., Fish, J. E., . . . Srivastava, D. (2008).
914 MicroRNA regulation of cell lineages in mouse and human embryonic stem cells. *Cell*
915 *Stem Cell, 2*(3), 219-229. doi:10.1016/j.stem.2008.01.016
916 Jan, C. H., Friedman, R. C., Ruby, J. G., & Bartel, D. P. (2011). Formation, regulation and
917 evolution of Caenorhabditis elegans 3'UTRs. *Nature, 469*(7328), 97-101.
918 doi:10.1038/nature09616
919 Kamath, R. S., & Ahringer, J. (2003). Genome-wide RNAi screening in Caenorhabditis
920 elegans. *Methods, 30*(4), 313-321. doi:10.1016/s1046-2023(03)00050-1
921 Lall, S., Grun, D., Krek, A., Chen, K., Wang, Y. L., Dewey, C. N., . . . Rajewsky, N. (2006). A
922 genome-wide map of conserved microRNA targets in C. elegans. *Curr Biol, 16*(5),
923 460-471. doi:10.1016/j.cub.2006.01.050
924 Liegeois, S., Benedetto, A., Garnier, J. M., Schwab, Y., & Labouesse, M. (2006). The V0-
925 ATPase mediates apical secretion of exosomes containing Hedgehog-related
926 proteins in Caenorhabditis elegans. *J Cell Biol, 173*(6), 949-961.
927 doi:10.1083/jcb.200511072
928 Lin, X. X., Sen, I., Janssens, G. E., Zhou, X., Fonslow, B. R., Edgar, D., . . . Riedel, C. G.
929 (2018). DAF-16/FOXO and HLH-30/TFEB function as combinatorial transcription
930 factors to promote stress resistance and longevity. *Nat Commun, 9*(1), 4400.
931 doi:10.1038/s41467-018-06624-0

Liu, N., Bezprozvannaya, S., Shelton, J. M., Frisard, M. I., Hulver, M. W., McMillan, R. P., . . . Olson, E. N. (2011). Mice lacking microRNA 133a develop dynamin 2-dependent centronuclear myopathy. *J Clin Invest, 121*(8), 3258-3268. doi:10.1172/JCI46267

Martinez, N. J., Ow, M. C., Reece-Hoyes, J. S., Barrasa, M. I., Ambros, V. R., & Walhout, A. J. (2008). Genome-scale spatiotemporal analysis of Caenorhabditis elegans microRNA promoter activity. *Genome Res, 18*(12), 2005-2015. doi:10.1101/gr.083055.108

Martinez, V. G., Javadi, C. S., Ngo, E., Ngo, L., Lagow, R. D., & Zhang, B. (2007). Age-related changes in climbing behavior and neural circuit physiology in Drosophila. *Dev Neurobiol, 67*(6), 778-791. doi:10.1002/dneu.20388

Miller, M. S., Lekkas, P., Braddock, J. M., Farman, G. P., Ballif, B. A., Irving, T. C., . . . Vigoreaux, J. O. (2008). Aging enhances indirect flight muscle fiber performance yet decreases flight ability in Drosophila. *Biophys J, 95*(5), 2391-2401. doi:10.1529/biophysj.108.130005

Miska, E. A., Alvarez-Saavedra, E., Abbott, A. L., Lau, N. C., Hellman, A. B., McGonagle, S. M., . . . Horvitz, H. R. (2007). Most Caenorhabditis elegans microRNAs are individually not essential for development or viability. *PLoS Genet, 3*(12), e215. doi:10.1371/journal.pgen.0030215

Mitchelson, K. R., & Qin, W. Y. (2015). Roles of the canonical myomiRs miR-1, -133 and -206 in cell development and disease. *World J Biol Chem, 6*(3), 162-208. doi:10.4331/wjbc.v6.i3.162

Morley, J. F., Brignull, H. R., Weyers, J. J., & Morimoto, R. I. (2002). The threshold for polyglutamine-expansion protein aggregation and cellular toxicity is dynamic and influenced by aging in Caenorhabditis elegans. *Proc Natl Acad Sci U S A, 99*(16), 10417-10422. doi:10.1073/pnas.152161099

Nair, K. S. (2005). Aging muscle. *Am J Clin Nutr, 81*(5), 953-963. doi:10.1093/ajcn/81.5.953

Nehammer, C., Ejlerskov, P., Gopal, S., Handley, A., Ng, L., Moreira, P., . . . Pocock, R. (2019). Interferon-beta-induced miR-1 alleviates toxic protein accumulation by controlling autophagy. *Elife, 8*. doi:10.7554/eLife.49930

O'Rourke, E. J., & Ruvkun, G. (2013). MXL-3 and HLH-30 transcriptionally link lipolysis and autophagy to nutrient availability. *Nat Cell Biol, 15*(6), 668-676. doi:10.1038/ncb2741

Panwar, B., Omenn, G. S., & Guan, Y. (2017). miRmine: a database of human miRNA expression profiles. *Bioinformatics, 33*(10), 1554-1560. doi:10.1093/bioinformatics/btx019

Perez-Riverol, Y., Csordas, A., Bai, J., Bernal-Llinares, M., Hewapathirana, S., Kundu, D. J., . . . Vizcaino, J. A. (2019). The PRIDE database and related tools and resources in 2019: improving support for quantification data. *Nucleic Acids Res, 47*(D1), D442-D450. doi:10.1093/nar/gky1106

Pollock, R. D., O'Brien, K. A., Daniels, L. J., Nielsen, K. B., Rowlerson, A., Duggal, N. A., . . . Harridge, S. D. R. (2018). Properties of the vastus lateralis muscle in relation to age and physiological function in master cyclists aged 55-79 years. *Aging Cell, 17*(2). doi:10.1111/acel.12735

Restif, C., Ibanez-Ventoso, C., Vora, M. M., Guo, S., Metaxas, D., & Driscoll, M. (2014). CeleST: computer vision software for quantitative analysis of C. elegans swim behavior reveals novel features of locomotion. *PLoS Comput Biol, 10*(7), e1003702. doi:10.1371/journal.pcbi.1003702

Rual, J. F., Ceron, J., Koreth, J., Hao, T., Nicot, A. S., Hirozane-Kishikawa, T., . . . Vidal, M. (2004). Toward improving Caenorhabditis elegans phenome mapping with an

ORFeome-based RNAi library. *Genome Res, 14*(10B), 2162-2168. doi:10.1101/gr.2505604

Sardiello, M., Palmieri, M., di Ronza, A., Medina, D. L., Valenza, M., Gennarino, V. A., . . . Ballabio, A. (2009). A gene network regulating lysosomal biogenesis and function. *Science, 325*(5939), 473-477. doi:10.1126/science.1174447

Settembre, C., Di Malta, C., Polito, V. A., Garcia Arencibia, M., Vetrini, F., Erdin, S., . . . Ballabio, A. (2011). TFEB links autophagy to lysosomal biogenesis. *Science, 332*(6036), 1429-1433. doi:10.1126/science.1204592

Settembre, C., Fraldi, A., Medina, D. L., & Ballabio, A. (2013). Signals from the lysosome: a control centre for cellular clearance and energy metabolism. *Nat Rev Mol Cell Biol, 14*(5), 283-296. doi:10.1038/nrm3565

Simon, D. J., Madison, J. M., Conery, A. L., Thompson-Peer, K. L., Soskis, M., Ruvkun, G. B., . . . Kim, J. K. (2008). The microRNA miR-1 regulates a MEF-2-dependent retrograde signal at neuromuscular junctions. *Cell, 133*(5), 903-915. doi:10.1016/j.cell.2008.04.035

Snel, B., Lehmann, G., Bork, P., & Huynen, M. A. (2000). STRING: a web-server to retrieve and display the repeatedly occurring neighbourhood of a gene. *Nucleic Acids Res, 28*(18), 3442-3444. doi:10.1093/nar/28.18.3442

Stark, A., Brennecke, J., Bushati, N., Russell, R. B., & Cohen, S. M. (2005). Animal MicroRNAs confer robustness to gene expression and have a significant impact on 3'UTR evolution. *Cell, 123*(6), 1133-1146. doi:10.1016/j.cell.2005.11.023

Tharyan, R. G., Annibal, A., Schiffer, I., Laboy, R., Atanassov, I., Weber, A. L., . . . Antebi, A. (2020). NFYB-1 regulates mitochondrial function and longevity via lysosomal prosaposin. *Nat Metab, 2*(5), 387-396. doi:10.1038/s42255-020-0200-2

Wang, S., Wong, L. Y., Neumann, D., Liu, Y., Sun, A., Antoons, G., . . . Luiken, J. (2020). Augmenting Vacuolar H(+)-ATPase Function Prevents Cardiomyocytes from Lipid-Overload Induced Dysfunction. *Int J Mol Sci, 21*(4). doi:10.3390/ijms21041520

Weber, J. A., Baxter, D. H., Zhang, S., Huang, D. Y., Huang, K. H., Lee, M. J., . . . Wang, K. (2010). The microRNA spectrum in 12 body fluids. *Clin Chem, 56*(11), 1733-1741. doi:10.1373/clinchem.2010.147405

Wust, S., Drose, S., Heidler, J., Wittig, I., Klockner, I., Franko, A., . . . Braun, T. (2018). Metabolic Maturation during Muscle Stem Cell Differentiation Is Achieved by miR-1/133a-Mediated Inhibition of the Dlk1-Dio3 Mega Gene Cluster. *Cell Metab, 27*(5), 1026-1039 e1026. doi:10.1016/j.cmet.2018.02.022

Xu, J., Cao, D., Zhang, D., Zhang, Y., & Yue, Y. (2020). MicroRNA-1 facilitates hypoxia-induced injury by targeting NOTCH3. *J Cell Biochem, 121*(11), 4458-4469. doi:10.1002/jcb.29663

Zhang, C. S., Jiang, B., Li, M., Zhu, M., Peng, Y., Zhang, Y. L., . . . Lin, S. C. (2014). The lysosomal v-ATPase-Ragulator complex is a common activator for AMPK and mTORC1, acting as a switch between catabolism and anabolism. *Cell Metab, 20*(3), 526-540. doi:10.1016/j.cmet.2014.06.014

Zhao, Y., Ransom, J. F., Li, A., Vedantham, V., von Drehle, M., Muth, A. N., . . . Srivastava, D. (2007). Dysregulation of cardiogenesis, cardiac conduction, and cell cycle in mice lacking miRNA-1-2. *Cell, 129*(2), 303-317. doi:10.1016/j.cell.2007.03.030

## Acknowledgements

AA would like to thank the MPI-AGE proteomics and imaging cores for services, the Caenorhabditis Genetics Center (CGC, University of Minnesota) for worm strains, the Bundesministerium für Bildung und Forschung for Sybacol funding, the Deutscher Akademischer Austauschdienst for funding, and the Max Planck Gesellschaft for core institutional support. MAM would like to thank Fundação de Amparo à Pesquisa do Estado de São Paulo (FAPESP) (Grant number 2019/25958-9) and Coordenação de Aperfeiçoamento de Pessoal de Nível Superior CAPES (Grant number 88881.143924/2017-01) for funding.

## Contributions

IS, BG, KK, RL, JH, MSD, YS, AA designed and performed experiments

IS, BG, SV, OS, AA wrote the paper

# Supplementary data

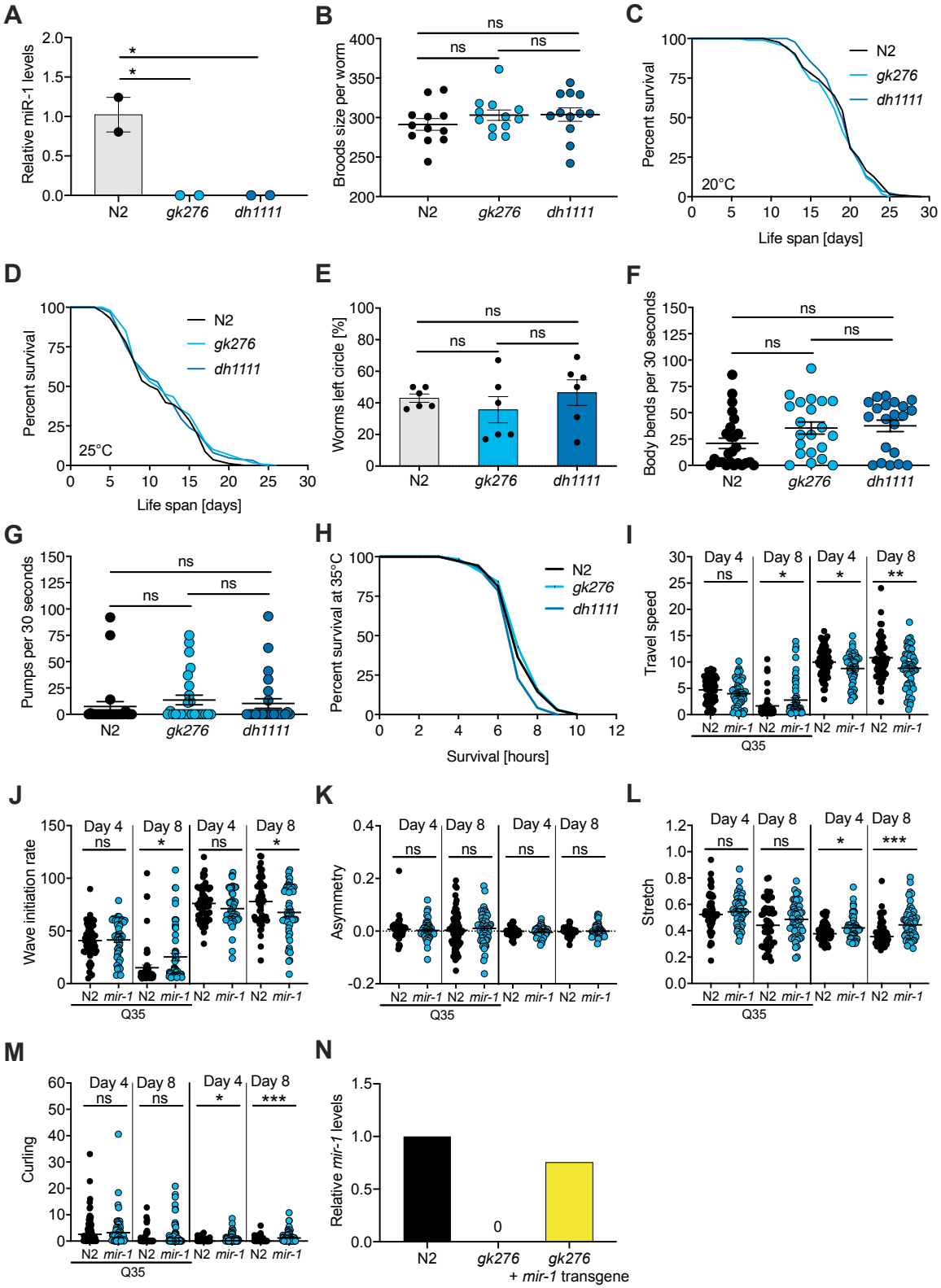


## Supplementary Figure 1. (linked to Figure 1)

**(A)** TaqMan qPCR measuring mature *mir-1* levels show that the deletion alleles do not express *mir-1* and are null, N=2 BR. mean ± SEM, one way ANOVA, *, p<0.05.

**(B)** Brood size of *mir-1(gk276)* and *mir-1(dh1111)* compared to wild-type (N2). Each dot represents the brood size of one worm, mean ± SEM, one way ANOVA, ns, not significant.

**(C)** and **(D)** Lifespan experiments performed at 20°C and 25°C for two *mir-1* deletion alleles compared to wild-type. N=3. Not significant (Supplemental Table 1).

**(E)** and **(F)** Motility of wild-type and *mir-1(gk276)* mutant animals on day 14 of adulthood, measured by circle test (E) and thrashing in liquid (F). One representative experiment of each N=3 is shown. Mean ± SEM, one way ANOVA, ns, not significant.

**(G)** Pharyngeal pumping rate measured on day 14 in two *mir-1* alleles compared to wild-type. N=3, one representative experiment is shown. Mean ± SEM, one way ANOVA, ns, not significant.

**(H)** Heat stress survival at 35°C of day 1 *mir-1(gk276)* and *mir-1 (dh1111)* mutants compared to wild-type. One representative experiment is shown, N=3, t-test: N2 *vs. gk276*: p=0.20. N2 *vs. dh1111*: p=0.17.

**(I)** to **(M)** CeleST locomotion behaviour analyses of wild-type and *mir-1(gk276)* mutant animals with or without *unc-54p::Q35::YFP*, at day 4 and day 8 of adulthood. Each dot represents one animal. **(I)** travel speed **(J)** wave initiation rate **(K)** asymmetry **(L)** stretch, and **(M)** curling. t-test, *, p<0.05, **, p<0.01, ***, p<0.001, ns, not significant.

**(N)** Bar graph showing the expression level of mature miR-1 microRNA in the indicated genotypes. N=1 biological replicate, 4 technical replicates.

A

| Target | miR-1 BS | Screen |
|---|---|---|
| *vha-1* | 1 | B |
| *vha-2* | 1 | (B) |
| *vha-3* | 1 | (B) |
| *vha-4* | 1 | B |
| *vha-5* | 1 | B |
| *vha-8* | 2 | B |
| *vha-9* | 1 | B |
| *vha-10* | 1 | B, P |
| *vha-11* | 2 | (B) |
| *vha-12* | 2 | B |
| *vha-13* | 2 | B |
| *vha-14* | 1 | B |
| *vha-15* | 2 | B |
| *vha-16* | 1 | (B) |
| *vha-17* | 1 | B |
| *vha-19* | 1 | (B), P |

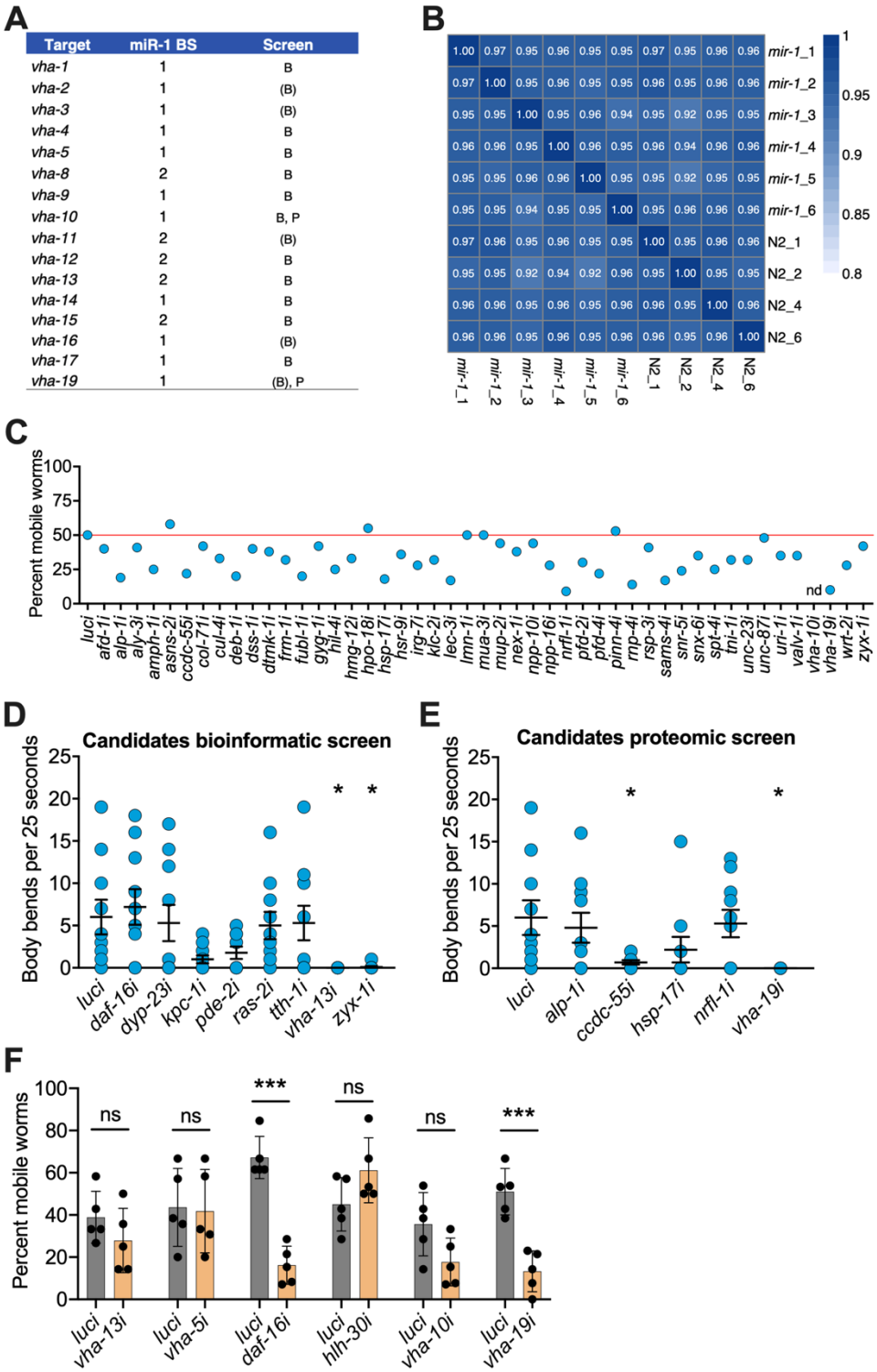


**Supplementary Figure 2. (linked to Figure 2)**

**(A)** v-ATPase subunits containing one or two predicted miR-1 binding sides (BS) in their 3'UTR. v-ATPase genes identified in the bioinformatic screen by all three databases are labelled „B", by 2 databases are labelled „(B)" and by the proteomic screen are labelled „P".

**(B)** Correlation plot of the biological replicates from proteomics showing the similarity of WT (N2) and *mir-1* genotypes.

**(C)** RNAi screen for genes required for *mir-1(gk276)*;Q35 motility in the circle test, using upregulated genes from the proteomic analysis (Supplemental Tables 5 and 6). Each dot represents the percentage of worms that left the circle. Red line, percent luciferase controls that left the circle. Nd, not determined. Validation of selected candidates identified from bioinformatic **(D)** and **(E)** proteomic screens by thrashing assay on day 8 of adulthood. *mir-1(gk276)*;Q35 worms were grown on the corresponding RNAi from L4 onwards. Each dot represents one animal, 15 worms per RNAi. Mean ± SEM, one way ANOVA, only significant values are labelled: *, $p<0.05$.

**(F)** Motility of worms in circle test of indicated RNAi on N2;Q35 worms. Motility was measured on day 5 of adulthood, each dot represents the percentage of worms that left the circle. Mean ± SEM of one representative experiment, N=3, one way ANOVA, ***, $p<0.001$, ns, not significant.

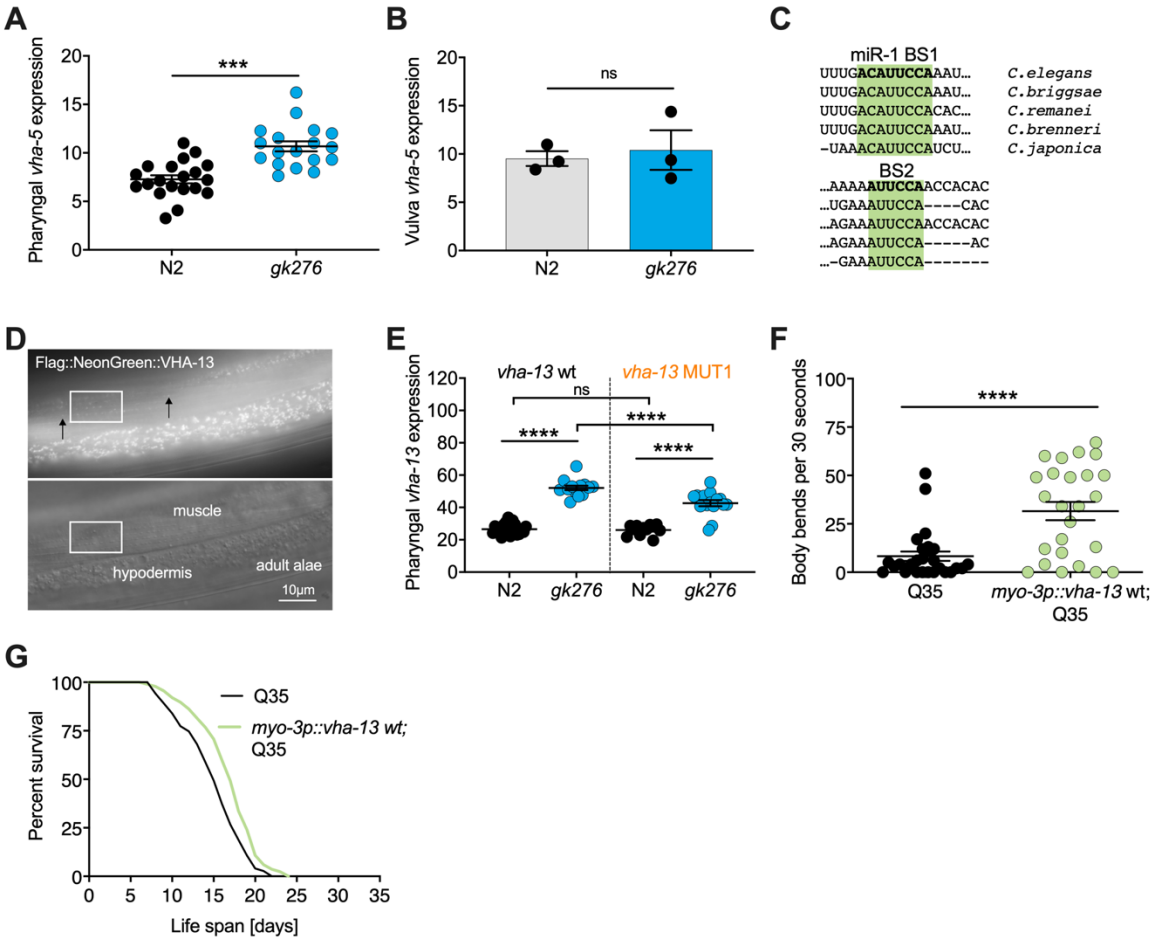


## Supplementary Figure 3. (linked to Figure 3)

**(A)** Quantification of pharyngeal fluorescent intensity of endogenous *3xFlag::mNeon Green::vha-5* expression in indicated genotypes in late L4s maintained at 25°C. One representative experiment of N=3, mean ± SEM, t-test, ***, p<0.001.

**(B)** Quantification of fluorescent intensity of *3xFlag::mNeonGreen::vha-5* expression in the vulva of indicated genotypes. Mean ± SEM of N=3, t-test, ns, not significant.

**(C)** Schematic showing the conservation of miR-1 binding sites (BS) in the *vha-13* 3'UTR of different nematode species.

**(D)** Images showing expression of endogenously tagged *3xFlag::mNeonGreen::vha-13* in muscle dense body and hypodermis. Arrows indicate individual dense bodies. Rectangle highlights muscle section shown in Figure 3B.

**(E)** Quantification of fluorescence intensity in the isthmus of L4 larvae with endogenously tagged *3xFlag::mNeonGreen::vha-13* with *vha-13* MUT1 3' UTR in relation to *vha-13* wt 3'UTR, in N2 and *mir-1(gk276)* mutant backgrounds using confocal microscopy. Mean ± SEM of one representative experiment. N=2, one way ANOVA, ****, p<0.00001, ns not significant.

**(F)** Thrashing assay of *unc-54p::Q35::YFP* (Q35) worms expressing *vha-13* in body wall muscle (*myo3p*::*vha-13* wt;Q35) or non-transgenic Q35 animals. 25 worms per genotype, mean ± SEM of one representative experiment, N=4, t-test, ****, p<0.0001.

**(G)** Life span of Q35 worms overexpressing *vha-13* in the body wall muscle (*myo3p*::*vha-13* wt;Q35) and Q35 non-transgenic segregants of the same strain. One experiment of N=4. Life span effects of two experiments were significant (Supplemental Table 1). t-test: 0.0017.

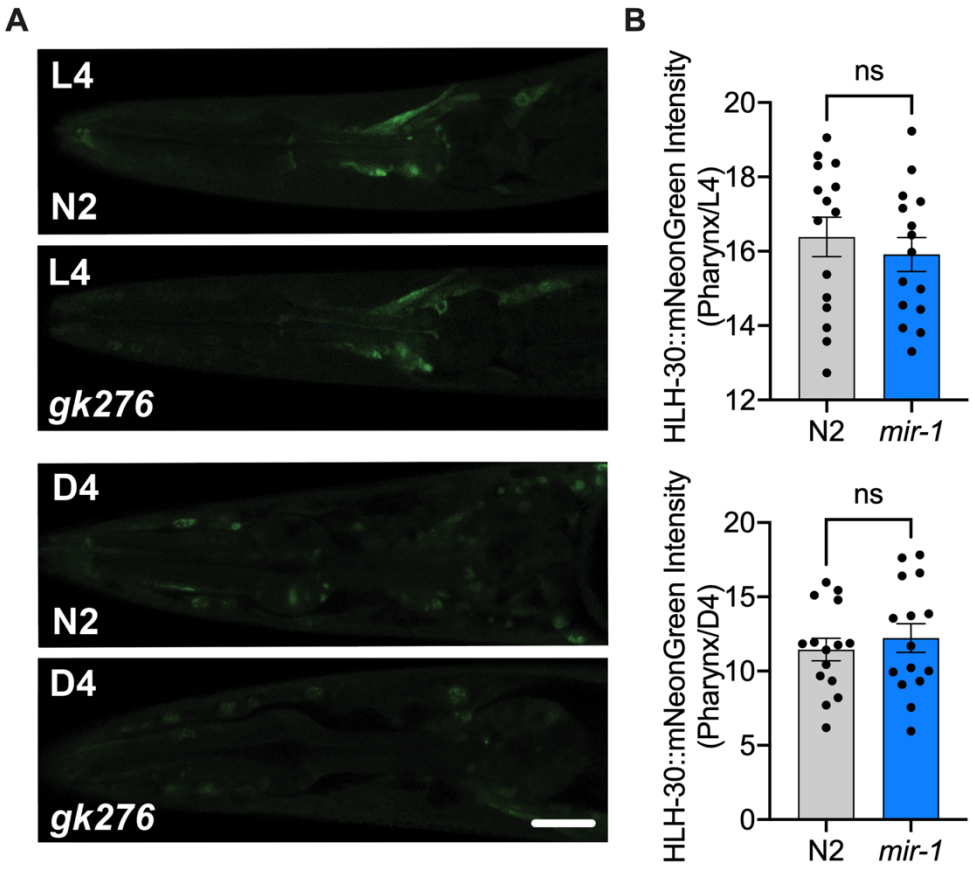


**Supplementary Figure 4. (linked to Figure 4)**

**(A)** Fluorescent image comparing HLH-30::mNeonGreen intensity in the pharynx of the *mir-1(gk276)* and WT (N2) backgrounds in L4s (top) or day 4 adults (D4, bottom). Scale bar 20 μm **(B)** Quantitation of nuclear localization in **(A)**, dots represent individual animals. N=2 biological replicates for L4 and N=1 for day 4 adults, t-test, ns: not significant.

Supplemental Table 1: Lifespan and heat stress data.

Supplemental Table 2: Q35 aggregate and behavior data.

Supplemental Table 3: CeleSt data.

Supplemental Table 4: Bioinformatic screen data.

Supplemental Table 5: RNAi motility screen.

Supplemental Table 6: Proteomic analysis of differentially regulated proteins in *mir-1* *vs.* wildtype.

Supplemental Table 7: Microscopy data.

Supplemental Table 8: Primers.